SARS-CoV-2 airway infection results in the development of somatosensory abnormalities in a hamster model

Randal A. Serafini[1,‡], **Justin J. Frere**[2,3,‡], **Jeffrey Zimering**[1,4], **Ilinca M. Giosan**[1], **Kerri D. Pryce**[1], **Ilona Golynker**[3], **Maryline Panis**[3], **Anne Ruiz**[1], **Benjamin R. tenOever**[3,*], **Venetia Zachariou**[1,5,6,*]

[1]Nash Department of Neuroscience and Friedman Brain Institute, Icahn School of Medicine at Mount Sinai, New York, NY 10029, USA.

[2]Department of Microbiology, Icahn School of Medicine at Mount Sinai, New York, NY 10029, USA.

[3]Department of Microbiology, New York University Grossman School of Medicine, New York, NY 10016, USA.

[4]Department of Neurosurgery, Icahn School of Medicine at Mount Sinai, New York, NY 10029, USA.

[5]Department of Pharmacological Sciences, Icahn School of Medicine at Mount Sinai, New York, NY 10029, USA.

[6]Department of Pharmacology, Physiology and Biophysics, Boston University Chobanian and Avedisian School of Medicine, Boston, MA 02118, USA.

Abstract

Although largely confined to the airways, SARS-CoV-2 infection has been associated with sensory abnormalities that manifest in both acute and chronic phenotypes. To gain insight on the molecular basis of these sensory abnormalities, we used the golden hamster model to characterize and compare the effects of infection with SARS-CoV-2 and Influenza A virus (IAV) on the sensory nervous system. We detected SARS-CoV-2 transcripts but no infectious material in the cervical and thoracic spinal cord and dorsal root ganglia (DRGs) within the first 24 hours of intranasal virus infection. SARS-CoV-2–infected hamsters exhibited mechanical hypersensitivity that was milder but prolonged compared to that observed in IAV-infected hamsters. RNA sequencing analysis of thoracic DRGs 1 to 4 days after infection suggested perturbations in predominantly neuronal signaling in SARS-CoV-2–infected animals as opposed to type I interferon signaling

*Corresponding author. Benjamin.tenOever@nyulangone.org (B.t.), vzachar@bu.edu (V.Z.).
‡These authors contributed equally.

in IAV-infected animals. Later, 31 days after infection, a neuropathic transcriptome emerged in thoracic DRGs from SARS-CoV-2–infected animals, which coincided with SARS-CoV-2–specific mechanical hypersensitivity. These data revealed potential targets for pain management, including the RNA-binding protein ILF3, which was validated in murine pain models. This work elucidates transcriptomic signatures in the DRGs triggered by SARS-CoV-2 that may underlie both short- and long-term sensory abnormalities.

INTRODUCTION

COVID-19, the disease resulting from SARS-CoV-2 infection, is associated with highly variable clinical outcomes that range from asymptomatic disease to death. For milder infections, COVID-19 is associated with respiratory infection-associated symptoms (cough, congestion, fever) and sensory phenotypes such as headache and anosmia (1–3). In more severe cases, however, SARS-CoV-2 infection can induce a variety of systemic perturbations that can affect nearly every organ, including strokes from vascular occlusion, cardiovascular damage, and acute renal failure (4–6). A substantial number of actively infected patients suffering from both mild and severe infections experience sensory-related symptoms, such as headache, visceral pain, Guillain-Barre syndrome (GBS), nerve pain, and polyneuritis (7–9). Whereas these symptoms subside after clearance of infection in most patients, they have been noted to arise in or persist to sub-acute or chronic timepoints for many others (10, 11). Sensory-related symptomology is thus a major component of this condition known as post-acute sequelae COVID-19 (PASC), or long COVID, defined by the World Health Organization as the persistence of COVID-19-associated symptomology that lasts for at least two months and cannot be explained by an alternative diagnosis (12). Accordingly, high persistence of abdominal, chest, and muscle pains, as well as headaches, was observed in patients with long COVID (13–15). Of note, the medical field has observed a high prevalence of asymptomatic, acute COVID-19 cases, suggesting a mechanistic divergence between the acute and chronic stages of the disease (16, 17).

Abnormal somatosensation is a common symptom of neuroinvasive and non-neuroinvasive viral infections, including varicella-zoster virus, human immunodeficiency virus (HIV), influenza A/B viruses, and SARS-CoV-2 (18–22). Phenotypes generally consist of painful sensations (burning, prickling, or aching), as well as paresthesias (tingling) or in some cases hypoesthesias (numbness). The mechanisms underlying these symptoms vary by virus. For example, certain neurotropic viruses, such as herpesviruses, persist in the dorsal root ganglia (DRGs) and directly induce abnormal activity in these primary sensory cells upon reactivation (23, 24). Retroviruses, such as HIV, can induce primary sensory neuropathy through viral protein interaction with axons while also inducing secondary inflammation at these neural sites, thereby inducing hyperexcitability and chronic pain symptoms (25, 26). However, the mechanisms by which coronaviruses, and specifically SARS-CoV-2, induce abnormal somatosensation are less understood (27).

The ability of SARS-CoV-2 to pass the blood-brain barrier and directly infect the central nervous system (CNS) is currently unclear. Whereas ultrastructural analyses of post-mortem tissue from COVID-19 patients have identified structures resembling viral particles in

the CNS, other studies have failed to detect replication-competent virus in the brain (28–32). These seemingly disparate results may be explained by pre-clinical studies in the golden hamster model of SARS-CoV-2 infection that demonstrate the presence of viral RNA in various brain regions—including the olfactory bulb, cortical areas, brainstem, and cerebellum—during active infection, despite lacking evidence for any infectious material in these regions (33, 34). Together, these data suggest that virus replication in the airways results in the dissemination of viral RNA, along with other potential inflammatory debris from the infection, leading to the induction of an antiviral transcriptional response in distal tissues, including the brain, which may underly CNS-related pathologies (such as demyelinating lesions and brain hemopathologies) that are observed among COVID-19 patients (35–38).

Despite the large number of studies investigating CNS infiltration during SARS-CoV-2 infection, little clinical or pre-clinical literature has investigated penetration capabilities of SARS-CoV-2 into the peripheral nervous system, particularly sensory components such as the DRGs. Though several case studies have highlighted peripheral fiber neuropathies in COVID-19 patients and in individuals who have recovered from the infection (39, 40), there is conflicting data regarding the presence of viral transcripts in the cerebrospinal fluid of COVID-19 patients (41–44).

Previous work with other members of the coronavirus family, including hemagglutinating encephalomyelitis virus (HEV), has identified active replication and satellite-mediated sequestration of virus in rodent DRGs (45). Mouse hepatitis virus also demonstrates anterior spinal cord segment invasion and persistence through neuroanatomical pathways such as the olfactory bulb and trigeminal ganglia, leading to consequences such as demyelination (46, 47). In these studies, the source of coronavirus-induced neurological dysfunction was linked to two major causes: direct virus-induced damage and collateral damage to host cells by anti-viral immune responses (48, 49). The cause of SARS-CoV-2-linked sensory pathologies is currently unknown, but SARS-CoV-2 can infect human neuronal cells in vitro (50–52) and induces a robust in vivo systemic inflammatory response (33, 34). Both findings could present causal mechanisms underlying SARS-CoV-2–linked sensory symptoms.

We hypothesized that clinically observed somatosensory symptoms (both positive and negative) arise from the exposure of neurons in the DRG and/or spinal cord to mature virus and/or circulating inflammatory materials, including cytokines and pathogen-associated molecular patterns (PAMPs). To test this hypothesis, we used the Syrian golden hamster model of viral respiratory infection, which accurately phenocopies COVID-19 in the absence of any virus or host adaptation (33, 34, 53), and longitudinally assessed gene and protein changes in sensory tissues of the spinal cord after infection with SARS-CoV-2, as compared to influenza A virus (IAV), and their association with mechanical hypersensitivity. Our findings provide insights into the sensory-altering mechanisms induced by respiratory SARS-CoV-2 infection and have the potential to guide the development of novel therapeutics for this and various other pain conditions.

RESULTS

SARS-CoV-2 RNA infiltrates thoracic and cervical DRG and spinal cord tissue

We first sought to determine whether SARS-CoV-2 genetic material was present in the sensory nervous system tissues and to investigate if this presence was associated with induction of an antiviral response. To this end, we performed a longitudinal cohort study in which hamsters were treated intranasally with SARS-CoV-2 or PBS (henceforth referred to as mock-infected or mock-treated). Cervical and thoracic regions of DRGs and spinal cord tissue (SC) were harvested at 1, 4, 7, and 14 days after infection (dpi) in both groups and assessed for the presence of SARS-CoV-2 subgenomic nucleocapsid protein (*N*) and canonical type-I interferon (IFN)-stimulated gene *Isg15* transcripts using quantitative reverse transcription-based quantitative PCR (qPCR). We found a substantial increase in the expression of *N* transcripts and of *Isg15* mRNA, which is generally representative of IFN signaling (54), at 1 dpi in cervical DRGs and SC (Fig. 1, A to D, and Table S2) and in thoracic DRGs and SC (Fig. 1, E to H). Both viral RNA and *Isg15* expression was cleared or returned to baseline, respectively, in most samples by 4 to 7 dpi.

To gain insight into viral replication within the DRG, we performed a plaque assay in which combined cervical and thoracic DRGs or SC were collected at 3 dpi and homogenized in PBS. This cell-homogenate solution was then plated with Vero cells, with the number of ensuing plaques representing the number of mature virions present in the harvested tissue. Plaques were observed only in 3-dpi lung homogenates from SARS-CoV-2-infected animals, but not in those from mock-treated animals or any DRG or SC tissue (Fig. 1I). This suggested that mature virus was not reaching the peripheral or central sensory nervous systems.

We next sought to determine whether SARS-CoV-2 transcripts were localized to specific cell types in the DRG, which is predominantly composed of primary sensory neurons and satellite glial cells. Using RNAscope in situ hybridization on 1-dpi cervical and thoracic cell tissue, we observed the presence of RNA (*S*) puncta around DAPI-labeled nuclei, which in DRGs are representative of satellite glial cells, and *Rbfox3*-labeled neuronal spaces in tissues retrieved from SARS-CoV-2-infected animals. *S* puncta were not present in tissues retrieved from mock-treated animals (Fig. 2A). We also detected *S* transcript puncta near DAPI signal throughout SARS-CoV-2-infected cervical and thoracic SC sections on 1 dpi. These puncta were not visible in SC tissues from mock-infected animals (Fig. 2B).

Of note, when tissue sections obtained from the DRGs of SARS-CoV-2–infected or mock-treated hamsters were immuno-labeled for SARS-CoV-2 nucleocapsid protein (NP) at 1 dpi, we did not observe any notable viral protein presence (Fig. 2C). We confirmed the presence of NP in SARS-CoV-2–infected lung samples at this time point and the lack thereof in mock-infected controls (Fig. 2C). This introduced the question of whether the presence of viral mRNA and associated antiviral response molecules in the sensory nervous system are sufficient to induce behavioral and/or transcriptional perturbations.

SARS-CoV-2 and IAV induce unique mechanical hypersensitivity signatures

We next sought to determine whether the presence of SARS-CoV-2 RNA or associated type I interferon (IFN-I) signaling, as reported previously (55), was associated with the induction of sensory hypersensitivity. To assess this, we performed the monofilament test on hamsters infected with either IAV (influenza A/California/04/2009) or SARS-CoV-2 and compared them to mock-infected hamsters. Similar to SARS-CoV-2, IAV is an RNA virus of the respiratory tract that is known to provoke a systemic inflammatory response similar to SARS-CoV-2, resulting in clinically-associated myalgias (34, 56). Mechanical withdrawal thresholds were measured during the acute phase of infection (1 and 4 dpi) to identify the effects of active and subsiding SARS-CoV-2 mRNA presence and IFN-I response on sensation. We observed a significant interaction effect between time and virus on mechanical hypersensitivity: IAV induced robust hypersensitivity at 1 dpi which completely subsided by 4 dpi, whereas SARS-CoV-2 infection instead resulted in a gradual reduction of withdrawal thresholds, reaching significance only at 4 dpi (Fig. 3A). Notably, IAV-induced hypersensitivity at 1 dpi was significantly more pronounced than that caused by SARS-CoV-2 in the same time frame. Considering the emergence of distinct behavioral signatures irrespective of systemic IFN responses induced by these two viruses, we performed a time-dependent transcriptional comparison of DRGs from SARS-CoV-2- and IAV-infected hamsters.

DRG transcriptional response to SARS-CoV-2 infection

We conducted transcriptional profiling using RNA-seq of thoracic DRGs (tDRGs) from SARS-CoV-2-, IAV-, and mock-infected hamsters at both 1 and 4 dpi because of their respiratory, visceral, and dermal innervations. Differential expression analysis of RNA-seq data revealed transcriptomic changes in tDRGs from both SARS-CoV-2- and IAV-infected hamsters compared to tDRGs from mock-infected hamsters at 1 and 4 dpi. SARS-CoV-2 infection resulted in a more robust differential expression (P-adj. < 0.1) at both time points: 344 genes at 1 dpi (271 up, 79 down) and 63 genes at 4 dpi (52 up, 11 down). IAV infection resulted in differential expression of 82 genes at 1 dpi (79 up, 3 down) and 18 genes at 4 dpi (9 up, 9 down) (Fig. 3B). Considering the milder acute mechano-sensitivity phenotype in SARS-CoV-2-infected hamsters and greater differential gene expression compared to IAV-infected hamsters, we hypothesized that certain acute SARS-CoV-2-induced transcriptional changes may counteract IFN-induced somatosensory sensitization, potentially by causing a stronger neuronal gene adaptation signature. To better assess this, we performed an Ingenuity Pathway Analysis (IPA) canonical pathway prediction on our RNA-seq data. This analysis showed neuron-specific transcriptional differences within the reported greatest upregulated canonical pathways (based on genes with nominal statistical significance of $P < 0.05$) (Fig. 3C). The top two most enriched pathways from SARS-CoV-2 tissue at 1 dpi were "Axonal Guidance Signaling" and "Synaptogenesis Signaling." At 4 dpi, "Neuroinflammation Signaling" was among the top five pathways. However, for IAV samples, the top canonical pathway results were consistently representative of generic viral response pathways.

To better understand which transcripts were driving these enriched annotations, we compared differentially expressed genes with adjusted significance (DEGs; P-adj. <

0.1) between tissues derived from IAV- and SARS-CoV-2-infected hamsters. Commonly upregulated genes between 1 and 4 dpi SARS-CoV-2 and IAV tissues were primarily anti-viral in nature, with only one co-downregulated gene emerging at 4 dpi, *Svep1* (a vascular-associated gene whose locus has been associated with poor SARS-CoV-2 clinical outcomes (57)) (Fig. 3D). RNA-seq was validated at 1 and 4 dpi through qPCR measurement of neuronal and anti-viral genes from SARS-CoV-2- and mock-infected tissues. Notably, we observed bi-directional regulation of neuropathy-associated and/or pro-nociceptive genes at 1 dpi, such as upregulation of *Sema3b* (58) and *Vegfa* (59, 60) and downregulation of *Rgs4* (61) (Fig. 3E). qPCR validations of 4 dpi included upregulation of *Mx1* and *Irf7* (pro-inflammatory, anti-viral genes) (62), as well as *Slc6a4* (63) and *Rgs18* (64), which have also been implicated in sensory abnormalities (Fig. 3E).

Analysis of upstream regulators (URs) of DEGs (*P*-nominal < 0.05) on IPA revealed several commonly and several oppositely regulated URs between SARS-CoV-2 and IAV datasets. Based on our hypothesis that SARS-CoV-2 transcriptionally counteracts IFN-induced hypersensitivity, we wanted to identify URs that were uniformly associated with timepoints of acute viral infection during which lower levels of hypersensitivity were observed, namely at 1 and 4 days after SARS-CoV-2 infection and 4 days after IAV infection. We focused on URs with predicted downregulated activity to identify molecular pathways that could be inhibited in order to alleviate sensory hypersensitivity. Nine URs met this criterion: Interleukin 6 receptor (IL6R), mitogen-activated protein kinase kinase (MEK), interleukin enhancer-binding factor 3 (ILF3), runt-related transcription factor 2 (RUNX2), protein kinase AMP-activated catalytic subunit α 2 (PRKAA2, or AMPKα2), follicle stimulating hormone (FSH), activating transcription factor 4 (ATF4), Snail family transcriptional repressor 1 (SNAI1), and inhibin subunit α (INHA) (Fig. 3F). Notably, pre-clinical and clinical literature supports a positive association between upregulation/activation of IL6R (65–67), MEK (68–70), RUNX2 (71, 72), FSH (73), and ATF4 (74, 75) and nociceptive states, and several laboratories have validated interventions in relevant pathways as promising anti-nociceptive therapeutic strategies. Only AMPKα2 activity was expressed toward a pro-nociceptive direction in this list, as pre-clinical literature suggests activation of this protein is associated with the alleviation of nociceptive symptoms (76, 77). These data suggest that other targets in this list may serve as novel therapeutic avenues of pain management. Among the identified genes that have not been studied in pain models (SNAI1, ILF3, and INHA), we chose to study ILF3 as there is a commercially available inhibitor, YM155, that can be systemically applied and has been clinically tested in patients with various cancers (78–80).

Predicted interactions between ILF3 and SARS-CoV-2-regulated genes further support its investigation as a pain target, as several genes were associated with either neuronal activity/plasticity (including *Fos, Col14a1, Aldh1a2, Fkbp5, Sema7a, Mgll Chi3l1,* and *Slc3a2*), or with interferon and cytokine responses (including *Isg15, Il1b, Il1rn, Tlr3, Tnc*) (fig. S1, A and B). To validate the directionality of predicted ILF3-targeting genes, we performed qPCR on *Fos* in 4 dpi tDRG tissue and found a significant downregulation (fig. S1C). As expected from the RNA-seq analysis, which did not characterize *Ilf3* as a significant DEG, whole-tissue qPCR demonstrated a lack of change in *Ilf3* gene expression in tissues from SARS-CoV-2- or IAV-infected hamsters from 1 or 4 dpi timepoints, suggesting that

changes in the activity of this molecule are occurring at the protein level (fig. S1D). Of note, YM155 is believed to affect subcellular localization of ILF3 and its associated complexes, as opposed to directly inhibiting its expression (81).

Inhibition of ILF3 activity alleviates sensory hypersensitivity in an inflammatory pain model

We next used the Complete Freund's Adjuvant (CFA) model of peripheral inflammation in female mice to determine the impact of ILF3 inhibition in sensory hypersensitivity behaviors associated with inflammatory pain states (Fig. 4A). We selected initial YM155 doses to test based on existing pre-clinical cancer literature, observing lethal toxicity at 20 mg/kg and variable toxicity at 10 mg/kg in female mice, so we proceeded with a 5 mg/kg once-daily regimen which did not cause obvious toxicity. This dose caused a trending reduction in locomotion at 20 min after injection, but locomotion was no different than that of vehicle mice by 30 min and onward (Fig. 4B). Accordingly, to identify any immediate analgesic effects of YM155 under local, peripheral inflammation conditions, we first tested CFA-injected mice in the monofilament and thermal withdrawal threshold testing at 30 min after drug administration. Compared to mock-treated mice, YM155-treated mice displayed increased thermal withdrawal times (Fig. 4C) and increased mechanical withdrawal thresholds (Fig. 4D). We also tested whether YM155 had sustained effects on sensory hypersensitivity after the expected window of activity (based on a õne hour half-life in intravenously-treated mice (82)). Indeed, when thermal withdrawal latencies were monitored at 24 hours after injection, we observed a significantly higher withdrawal latency at six consecutive days (PD-D6) of YM155 administration (Fig. 4E), prior to the expected recovery from thermal hypersensitivity in CFA animals. Similarly, we observed sustained recovery of mechanical thresholds on PD-D5, PD-D7, and PD-D9 in the Von Frey assay (Fig. 4F). We observed no changes in animal weight following YM155 administration over the first 9 days of treatment (Fig. 4G).

Because the CFA model promotes both peripheral interferon and cytokine signaling, we wanted to investigate the role of ILF3 inhibition in a model of isolated interferon signaling to better understand its role in virus-induced hypersensitivity. For this, we implemented hindpaw interferon β (IFN-β) injections. We first replicated the findings by Barrágan-Iglesias *et al.* in male mice (55), wherein 300U in a 25 μL intraplantar injection produced reliable hypersensitivity in ipsilateral (injected) versus contralateral (naïve) hindpaws by one day after injection and persisted until at least three days after injection (Fig. 4H). We next compared mechanical thresholds between a group of female mice that received no IFN-β injection and daily saline (naïve-saline), a group that received a single IFN-β injection and daily saline (IFN-β-saline), and a group that received a single IFN-β injection and immediate daily administration of YM155 (5 mg/kg intraperitoneal twice-daily; IFN-β-YM155). On days 1 and 3 after IFN-β administration, we observed robust mechanical hypersensitivity in the IFN-β-saline group, but no change in thresholds in the IFNβ-YM155 group, suggesting that ILF3 inhibition attenuates interferon-induced hypersensitivity (Fig. 4I). When testing YM155 in male mice, we noted increased sensitivity to the drug and subsequent toxicity at the 5 mg/kg dose. We therefore performed an experiment in which a naïve-saline and IFN-β-saline group began receiving YM155 (2.5 mg/kg intraperitoneal

twice-daily) after mechanical thresholds were taken one day after intraplantar injections. At this dose, we observed neither toxicity nor changes in the naïve group's withdrawal thresholds, whereas we noted a substantial increase in mechanical thresholds in the IFN-β-treated group by the third day after intraplantar injections (Fig. 4J). This suggests that, although sex-specific dose optimization may be necessary, ILF3 inhibition is effective at suppressing interferon-induced hypersensitivity independent of sex.

We also tested whether YM155 could be used to prophylactically reduce pain experienced after acute post-operative injuries to determine whether ILF3 inhibition could attenuate primary hyperalgesia due to both peripheral nerve-ending damage and local inflammation. For this, we used the paw incision model and pre-treated female mice at a dose of 5 mg/kg for seven days. Animals were not treated with drug after the incision operation. We observed a significant reduction in mechanical hypersensitivity due to the incision in the YM155-treated animals compared to vehicle-treated counterparts (Fig. 4K). Notably, we observed no changes in locomotor activity between animals immediately after testing mechanical hypersensitivity on the first day after injury (Fig. 4L).

SARS-CoV-2 induces a unique, persistent transcriptomic profile in DRGs

Given that the severity of sensory hypersensitivity during acute infection with SARS-CoV-2 worsens over time and the existence of persistent sensory symptoms in patients afflicted by long COVID, we set out to determine whether the hamster respiratory model of SARS-CoV-2 infection displayed any prolonged sensory phenotypes. In this set of studies, we assessed mechanical hypersensitivity in male and female SARS-CoV-2-, IAV-, and mock-infected hamsters 28 days after infection, well after viral clearance. We observed substantial mechanical hypersensitivity in SARS-CoV-2-infected hamsters of both sexes, but normal responses for IAV- and mock-infected hamsters (Fig. 5A).

To determine whether longitudinally-altered molecular mechanisms in the DRG may be responsible for this SARS-CoV-2-specific hypersensitivity phenotype, we performed RNA-seq analysis and compared 31 dpi thoracic DRGs between SARS-CoV-2- and mock-infected male animals. To our surprise, we identified 1065 DEGs (P-adj. < 0.1, 170 up, 895 down; Fig. 5B), consisting of a much larger number of DEGs than we observed with the 4-dpi thoracic DRGs from SARS-CoV-2-infected animals. Ontology analysis of DEGs (P-nominal < 0.05) also highlighted new and counter-regulated canonical pathways compared to those observed in 1 dpi and 4 dpi thoracic DRG tissues from SARS-CoV-2- and IAV-infected animals, including decreased "Synaptogenesis Signaling", and the involvement of "EIF2 Signaling", "mTOR Signaling", "Opioid Signaling", and "SNARE Signaling" (Fig. 5C). Furthermore, use of Enrichr's DisGeNET gateway primarily associated these DEGs with neuro-oncological and neurodegenerative conditions, including Glioblastoma, Alzheimer's Disease, Parkinson Disease, and Neurilemmoma (Fig. 5D). Key DEGs (those that were statistically different beyond the p-adj. threshold of 0.1) from the RNA-seq analysis supported our observed maladaptive alterations in canonical neuronal and inflammatory pathways, including changes in gene expression of several tubulin mRNA (*Tubb*) isoforms, myelin proteins, activity-related channels, extracellular matrix proteins, and cytokine/interferon-related proteins (Fig. 5E).

Analysis of predicted cell subtype influence on the 31 dpi tDRG transcriptomic signatures using RNA-seq deconvolution highlighted a reduced transcriptomic contribution from myelinating Schwann cells and increased contribution from macrophages in tissues harvested from SARS-CoV-2-infected hamsters compared to mock-infected hamsters (Fig. 5F), suggesting a SARS-CoV-2-associated pro-inflammatory state with potentially impaired myelination.

We next sought to determine whether a core group of URs may serve as a common target for sensory and perceptive components of pain, as well as affective comorbidities observed in patients with long COVID. We performed an IPA-based UR comparison analysis between our 31 dpi DRG, striatum, and thalamus RNA-seq data, the latter two datasets coming from another systemic analysis of long COVID model hamsters, under the same conditions, that we previously performed (34). The striatum and thalamus are regions of the brain involved in the initiation and maintenance of sensory components of pain as well as the emotional manifestations of pain (83, 84). The majority of the top 15 URs demonstrated a similarly predicted activation or inhibition state between the thalamus and striatum that was generally opposite the change seen in the DRGs (Fig. 5G). The genes encoding the protein tyrosine phosphatase family member PTPRR and the microRNA precursor *MIR17HG* were commonly upregulated, and the gene encoding the lncRNA FIRRE was commonly downregulated, in DRGs and the thalamus.

SARS-CoV-2 infection causes transcriptomic signatures in the DRGs that are similar to persistent inflammation and nerve injury models

Whereas our bioinformatic analysis of SARS-CoV-2 RNA-seq datasets identified potential treatment targets, such as ILF3, we also wanted to determine if a meta-analysis of these data against existing peripheral injury datasets may yield a more comprehensive list of pain targets. We therefore compared the 1, 4, and 31 dpi thoracic DRG RNA-seq data sets from SARS-CoV-2-infected hamsters against a publicly available RNA-seq data set from FASTQ files from Parisien *et al.*, which analyzed DRGs from mice exposed to CFA or spared nerve injury (SNI) (GSE111216; see Materials and Methods). We observed several commonly upregulated genes between SARS-CoV-2- and CFA-affected tissues at both 1 and 4 dpi, and only at 1 dpi between SARS-CoV-2- and SNI-affected tissues (Fig. 6A). Notably, we identified a group of 53 genes that were upregulated 1 day after SARS-CoV-2 infection but downregulated after SNI (Fig. 6A). Analysis with g:Profiler associated this gene set with neuroplasticity, particularly in the synaptic/dendritic cellular compartments, and strongly associated the transcription factor SP1 (implicated in several pro-nociceptive mechanisms) with these genes (Fig. 6B) (85–87). Some of these genes— such as *Scn4b* (88, 89), *Rhobtb2* (90), *Mgll* (91, 92), and *Cntfr* (93)—have been positively associated with sensory hypersensitivity in response to injury, suggesting they may be unique mechanisms by which SARS-CoV-2 induces mild hypersensitivity. This finding also highlights potential SNI-induced compensatory anti-nociceptive gene programs. However, several anti-nociceptive genes were also upregulated following SARS-CoV-2 infection, including *Gprc5b* (94) and *Grk2* (95, 96). Several genes implicated in neurodevelopment and dendritic plasticity were also upregulated by SARS-CoV-2 infection but, to our knowledge, have not yet been implicated in pain. Potentially interesting candidates include

Olfm1, Fxr2, Atcay, Cplx1, Iqsec1, Dnm1, Clstn1, Rph3a, Scrt1, Ntng2 and *Lhfpl4.* Ontologies that were statistically significantly associated with this SARS-CoV-2 versus SNI contra-regulated gene list (*P*-adj. < 0.1) are GO: Biological Pathway (GO:BP) nervous system development, GO:BP generation of neurons, GO: Cellular Component (GO:CC) somatodendritic compartment, GO:CC synapse, and GO:CC cell junction. We also identified a core set of genes, mostly associated with extracellular matrix remodeling, was commonly upregulated between 1 dpi SARS-CoV-2-, CFA-, and SNI-affected tissues: *Col1a1, Col1a2, Col6a3, Hspg2, Irgm, Lama2, Lamb1, Lamc1, and Siglec1* (Fig. 6C). This concurs with previous literature implicating extracellular matrix remodeling with the maintenance of inflammatory- and nerve injury-associated pain sensation (97).

Lastly, comparison of all genes regulated in CFA and 31 dpi SARS-CoV-2 conditions revealed a subset of counter-regulated (*P-adj. < 0.05)* DEGs (36 up in CFA, down in SARS-CoV-2; Fig. 6A). These genes are implicated in pathways such as myelination/ axon ensheathment (*Mpz, Mbp, Prx, Fa2h, Dhh,* and *Mag*), semaphorin-regulation of axonogenesis (*Sema3g* and *Sema4g*), and extracellular matrix organization (*Nid2, Col5a3, Mmp15, Mmp14, Col4a1,* and *Fscn1*) (GO:BP). We observed a strong transcriptional counter-regulation between SNI and 31 dpi SARS-CoV-2 conditions as well (89 up in SNI, down in SARS-CoV-2 down). This signature was predominantly related with nervous system development, with implicated genes including *Mpz, Plec, Prkcg Metrn, Slit1, Brd2, Anks1a, Cpne5, Sema4f, Hspg2, Sh3gl1, Prag1, Map6, Mdga1, Fphs, Ppp2r5b, Plod3, Phgdh, Dpysl5, Gpc1, Elavl3, Gpsm1, Marcksl1, Col4a1, Niban2, Carm1, Irs2, Lgi4, Erbb2, Syngap1,* and *Nlgn2* (GO:BP).

However, we were mostly surprised by the robust overlap of downregulated DEGs between the SNI and 31 dpi SARS-CoV-2 conditions (Fig. 6A). Nervous system development and morphogenesis were robust pathway signatures, implicating neuronal plasticity as a key contributor to nerve injury and virus-induced pain states. But this comparison also uniquely revealed strongly altered synaptic transmission pathways, with DEGs including *Slc7a7, Syngr1, Prkaca, Rab3a, Ntrk1, Nptx1, Stx1b, Jph3, Mapk8ip2, Calm3, Pnkd, Ppp1r9b, Pip5k1c, Cacng7, Dlgap3, Nrxn2, Pink1, Grk2, Ncdn, Cplx2, Camk2b, Grin1, Brsk1, Ache,* and *Jph4.* This gene list suggests that SARS-CoV-2 mirrors nerve injury-associated maladaptive mechanisms both through direct modification of neuronal excitability at the membrane level and through modulation of transcriptional regulation elements. Other commonly-associated pathways included β-amyloid binding and TRP channel modulation (Fig. 6D), which may be interesting to explore further.

DISCUSSION

The relatively high prevalence of both acute asymptomatic SARS-CoV-2 cases and positive somatosensory abnormalities in patients with long COVID prompted our group to investigate the ability of SARS-CoV-2 to perturb sensory nervous system functions. In the golden hamster model of COVID-19 (98, 99), we detected low levels of SARS-CoV-2-derived RNA in the spinal cord and DRG in the absence of infectious particles. The presence of this viral material in sensory tissues and/or the resulting type I interferon response and gene expression changes associated with neuronal maladaptations correlated with a

progressive and prolonged mechanical hypersensitivity signature that was unique to SARS-CoV-2-infected animals. Transcriptomic analysis of thoracic DRGs from SARS-CoV-2-infected hamsters highlighted a pronounced neuronal signature unlike the predominantly pro-inflammatory signature seen in DRGs from IAV-infected hamsters. SARS-CoV-2 infection also correlated with worsened hypersensitivity post-recovery in both female and male hamsters, which may be attributable to altered excitability, cytoskeletal architecture, extracellular remodeling, and myelination because of the host response to this inflammatory material. Transcriptional profiling of tDRGs at 1, 4, and 31 dpi implicated several potential therapeutic targets for the management of chronic pain. Indeed, the prediction of ILF3 inhibition as a potential therapeutic intervention was validated in murine CFA, IFN-β, and hindpaw incision models. Lastly, meta-analysis against existing transcriptional data sets from pain models highlighted several unexplored acutely and chronically contra-regulated genes between SARS-CoV-2 and SNI conditions that could serve as future targets for anti-nociceptive therapies and provide novel mechanistic insight into these perturbations.

The SARS-CoV-2 RNA infiltration dynamics within sensory tissue observed in this study were similar to those noted in our longitudinal study of the effects of SARS-CoV-2 on the brain, where a rapid transcriptional induction to infection is followed by a return to baseline in most, but not all tissues (34). Given the presence of SARS-CoV-2 RNA in various cell types of the DRG, we were surprised by the neuronally-biased transcriptional responses associated with this positivity that were not as prominent in tissue from IAV-infected hamsters. Together, these data suggest that the host response to SARS-CoV-2 infection elicits a unique transcriptional output capable of inducing lasting changes to DRG plasticity.

In addition to elucidating the impact SARS-CoV-2 has on DRGs, this study also identified a subset of host factors as modulators of the nociceptive responses. Of note, increased activity of ILF3 (100–102) is generally considered oncogenic. Furthermore, several of the disease risk signatures associated with gene changes observed in the 31 dpi SARS-CoV-2 DRGs revolved around neuronal and glial cancers. Given the success of using cancer-targeting therapies for the treatment of inflammatory- and nerve injury-associated pain states (83, 103, 104, 105), we believe that the careful repurposing of existing clinically validated cancer therapeutics may serve as one possible strategy for providing alternative treatments for pain management.

Future studies will focus on robust characterization of predicted pathways and validation of novel treatment interventions. For example, ephrin receptor signaling, which frequently appeared in our ontology analyses, has a documented role in nociceptive processing (106). Ephrin signaling is an essential mediator of extracellular phosphorylation states (107) and matrix dynamics (108), which subsequently affect synaptic plasticity in the form of neurite outgrowth and synaptic integrity (109). Current pain therapeutics are primarily focused on modulating maladaptive neuronal hyperexcitability by targeting GPCRs or ion channels (110). However, few interventions target downstream transcriptomic mechanisms that broadly influence synaptic plasticity, an essential component of central sensitization. Along with ILF3, upstream regulators of the SARS-CoV-2-activated ephrin pathway may support this alternative treatment direction.

RNA-seq cell subtype deconvolution also identified two cell populations that may disproportionately contribute to prolonged mechanical hypersensitivity after recovery from SARS-CoV-2: myelinating Schwann cells and macrophages. Macrophages play a substantial role in the initiation and maintenance of neuropathic pain (111–113), further emphasizing the potential efficacy of anti-inflammatory interleukins in persistent SARS-COV-2-induced hypersensitivity. The reduction in myelin-associated transcripts at 31 dpi may suggest a de-myelination-like phenotype, which is associated with hypersensitivity in other models, such as lysolecithin- and bortezomib-induced demyelination (114, 115).

Furthermore, few pain therapeutics target both the peripheral and central site of the nociceptive pathway. Here, we identified that several common predicted upstream regulator targets exist between the DRGs and brain regions that process pain and emotion. Whereas the expression of most of the top common upstream regulators were counter-regulated between the DRGs and the thalamus or striatum, three of those—the phosphatase PTPRR, microRNA precursor *MIR17HG*, and the lncRNA FIRRE—were predicted to change unidirectionally between the DRG and the thalamus. Although PTPRR has not been implicated in pain, human studies have suggested an association between its upregulation and depression (116, 117). Gene abnormalities in *MIR17HG* have also been reported in Feingold 2 syndrome patients that suffer from chronic myofascial pain and affective symptoms (118, 119), and FIRRE has been implicated in spinal cord neuropathic pain mechanisms (120). Thus, common regulators between the peripheral and central nervous systems may serve as useful targets for both sensory and affective symptoms of long COVID. Notably, in this study, the expression of the *Rgs4* gene was decreased at 1 dpi in DRGs of SARS-CoV-2-infected hamsters. This circuitry-wide analysis also bears relevance for systemic diseases, such as myalgic encephalitis/chronic fatigue syndrome (ME/CFS), whereby mechanisms that affect the entire nervous system, such as persistent inflammation, may not be attenuated by interventions targeting only one level of the pain matrix.

Lastly, our meta-analysis emphasized the ability of SARS-CoV-2 to recapitulate transcriptional perturbations in the DRG underlying both inflammatory- and nerve injury-associated pain states. However, these findings also demonstrate the induction of plasticity-associated perturbations that counter those seen in other injury models. Future studies will elucidate whether these differences promote the maintenance of mechanical hypersensitivity we observed in SARS-CoV-2-infected animals. Furthermore, these findings support the use of the SARS-CoV-2 respiratory infection hamster model as a preclinical chronic pain model, which can be used for the evaluation of pharmacological treatments.

Whereas several groups have recapitulated human COVID-19 symptoms in this respiratory hamster model, this study confirmed the model's relevance for somatosensory symptoms. From a mechanical hypersensitivity perspective, this model aligns with the somatosensory trajectory, both acute and chronic, of many COVID-19 patients. For example, our findings interestingly align with other hypotheses and reports that acute SARS-CoV-2 infection may attenuate existing pain or reduce expected myalgic hypersensitivity due to viral infection (60, 121) but may also result in prolonged pain symptoms (122). This SARS-CoV-2 model was also useful for further identifying core mechanisms across pain models while also

potentially providing insights into the viral-mediated nociceptive states that are relevant for drug development.

MATERIALS AND METHODS

Infection and Local-Inflammation Animal Models

One- to two-month-old male golden hamsters (*Mesocricetus auratus*) were used in all infection experiments, and age-matched female hamsters were included in the 31 dpi experiments (Charles River Laboratories, MA). Male hamsters were co-housed on a twelve-hour light-dark cycle and had access to food and water *ad libitum*. Female hamsters were housed individually to prevent injury due to aggression. Hamster work was performed in a CDC/USDA-approved biosafety level 3 laboratory in accordance with NYU Langone and Icahn School of Medicine at Mount Sinai IACUC protocols. For behavioral experiments, experimenters were blinded to treatment. Mice were housed on a twelve-hour light-dark cycle and had access to food and water *ad libitum* in accordance with the Icahn School of Medicine at Mount Sinai IACUC protocols.

Two- to three-month-old hamsters received an intranasal inoculation of 100μL of phosphate-buffered saline (PBS) containing 1000 plaque forming units (PFU) of SARS-CoV-2, 100,000 PFU of IAV (viral control), or PBS alone (negative control for infection conditions; referred to as "mock-infected" or "mock-treated" throughout the manuscript) (34, 123). Hamsters were euthanized by intraperitoneal pentobarbital injection followed by cardiac perfusion with 60 mL PBS.

For studies using models of peripheral inflammation, two- to three-month old mice received 30 μL left hindpaw injections of CFA (diluted 1:1 in saline) or IFN-β (300 U in 25 μL). For studies using the post-operative incision model, two- to three-month-old mice received an incision from the posterior plantar surface of the hindpaw to the middle of the paw pads, in which dermis and superficial muscle was cut and dermis was sutured afterwards as cited (124). CFA and paw incision groups of mice received daily intraperitoneal (i.p.) injections of saline (vehicle) or YM155 (Tocris Biosciences), an Interleukin Enhancer Binding Factor 3 (ILF3) inhibitor (5mg/kg diluted in saline).

Punctate Mechanical Threshold Testing

Hamsters or mice were placed on a raised grid platform in plastic containers and were allowed to habituate to their environment for a minimum of 10 minutes. Afterwards, filaments of ascending forces were applied to the left hindpaw and responses were recorded. A positive response consisted of a hindpaw lift, shake, or lick. Progression to the next filament was determined by recording positive or negative responses for three out of five applications with each filament. Mechanical withdrawal threshold was defined as the first (for hamsters, to minimize cross-contamination of cohorts by prolonged fomite exposure) or second (mouse, for consistency) filament force at which an animal had three positive responses. Whereas standard, logarithmic gram-based measurements were used for mice at low filament forces, we utilized linear "perceived intensity" values provided on the Semmes-Weinstein monofilaments (North Coast Medical, Inc.) to compensate for the measurement of

a low number of hamsters at high, variable forces, due to BSL3 restrictions. All materials utilized for testing infected hamsters were thoroughly decontaminated between groups.

Thermal Withdrawal Threshold Testing

The CFA model induces thermal hypersensitivity for 10–14 days on average (83). We used the Hargreave's thermal beam assay to assess the effects of YM155 administration on thermal hypersensitivity associated with left hindpaw CFA injection. Mice were placed on a Hargreave's platform in plastic containers and were allowed to habituate for 30 minutes. A light beam heat source (IITC Life Science Inc., CA) set to an intensity level of IF=30 was aimed at the left hindpaw for a maximum of 20 seconds (cutoff). Similarly to Von Frey, paw withdrawal was defined as a hindpaw lift, shake, or lick. Three measurements were recorded and averaged for each hindpaw, with each measurement taking place at least two minutes apart.

Locomotor Testing

The beam break assay was used to test locomotor activity in mice that received saline or YM155 (Med Associates Inc.). Animals received YM155 or vehicle either immediately before the initiation of the assay, or in animals that had been pre-treated at least 24 hours before. Animals were allowed to explore the cage for 60 min and the aggregate of all beam breaks was quantified for each animal in 10-min intervals.

Tissues

Tissues were harvested at 1, 4, and 31 dpi and immediately placed in TRIzol (Invitrogen, MA) for transcriptomic analysis or 4% paraformaldehyde (PFA) in phosphate-buffered saline (PBS) for histology or fluorescent in situ hybridization (RNAscope). Fixed tissues were sucrose converted after 48 hours of 4% PFA fixation in 10% sucrose in PBS (Day 1), 20% sucrose in PBS (Day 2), and 30% sucrose in PBS with 0.01% azide (Day 3). Slide-mounted tissues were paraffin-embedded and sliced to a thickness of 5 microns. Tissue collected for transcriptomic analysis were homogenized in Lysing Matrix A homogenization tubs (MP Biomedicals, CA) for two cycles (40s; 6m/s) in a FastPrep 24 5g bead grinder and lysis system (MP Biomedicals, CA). Tissue collected for plaque assays was homogenized in 1 mL PBS in Lysing Matrix A homogenization tubs (MP Biomedicals, CA) for two cycles (40s; 6m/s).

RNA Isolation and qPCR

RNA was isolated through a TRIzol:chloroform phase separation protocol as detailed in the TRIzol Reagent User Guide. RNA concentrations were measured by NanoDrop (Thermofisher, MA). 1,000ng of cDNA was synthesized using the qScript cDNA Synthesis kit (QuantaBio, MA) as detailed in the qScript cDNA Synthesis Kit Manual. Exon-exon-spanning primers targeting as many splice variants as possible were designed with Primer-BLAST (National Center for Biotechnology Information, Maryland, USA). qPCRs were performed in triplicate with 30 ng of cDNA and a master mix of exon-spanning primers (table S1) and PerfeCTa SYBR Green FastMix ROX (QuantaBio, MA) on an QuantStudio

real-time PCR analyzer (Invitrogen, MA), and results were expressed as fold change (2^{-Ct}) relative to the β-actin gene (*Actb*).

Plaque Formation Assay

Plaque assays were performed as described previously (33). Virus was logarithmically diluted in SARS-CoV-2 infection medium with a final volume of 200 μL volume per dilution. 12-well plates of Vero E6 cells were incubated for 1 hour at room temperature with gentle agitation every 10 min. An overlay comprised of Modified Eagle Medium (GIBCO), 4 mM L-glutamine (GIBCO), 0.2% BSA (MP Biomedicals), 10 mM HEPES (Fisher Scientific), 0.12% $NaHCO_3$, and 0.7% Oxoid agar (Thermo Scientific) was pipetted into each well. Plates were incubated at 37°C for 48 hours prior to fixation in 4% PFA in PBS for 24 hours. Plaques were visualized by staining with crystal violet solution (1% crystal violet (w/v) in 20% ethanol (v/v)) for 15 min.

RNAscope In Situ Hybridization

The Fluorescent Multiplex V2 kit (Advanced Cell Diagnostics, CA) was used for RNAscope FISH. Specifically, we used the FFPE protocol as detailed in the RNAscope Multiplex Fluorescent Reagent Kit v2 Assay User Manual. RNAscope probes were as follows: *Rbfox3* (NeuN) for pan-neuronal labeling (Mau-Rbfox3-C1) and the Spike gene (*S*) for SARS-CoV-2 labeling (V-nCoV2019-S-C3). Opal dyes (Akoya Biosciences, MA) were used for secondary staining as follows: Opal 690 for C1 and Opal 570 for C3. DAPI was used for nuclear staining. Images were taken on an LSM880 confocal microscope (Zeiss, GER) with identical parameters between mock and SARS samples.

Immunohistochemistry

Immunohistochemistry was performed according to protocols described previously (34). Briefly, 5 μm sections were cut from FFPE tissues and mounted on charged glass slides. Sections were deparaffinized by immersion in xylene and subsequently submerged in decreasing concentrations of ethanol to rehydrate. Rehydrated sections were submerged in IHC-Tek Epitope Retrieval Solution (Cat #IW-1100) and steamed for 45 min in IHC-Tek Epitope Retrieval Steamer (Cat #IW-1102) for antigen retrieval. Tissues were blocked with 10% goat serum and 1% bovine serum albumin in TBS for 1 hour at room temperature. Primary antibody (monoclonal murine-derived anti-SARS-CoV-2 N protein) was diluted 1:100 in a 1% BSA TBS solution and added to slides. Slides were incubated with primary antibody solution overnight at 4°C. Slides were washed in TBS with 0.025% Triton-X-100 and treated with 0.3% hydrogen peroxide in TBS for 15 min. Slides were washed once again. HRP-conjugated goat anti-mouse IgG secondary antibody (ThermoFisher, Cat #A21426) was diluted 1:5000 and added to slides. Slides incubated with secondary antibody at room temperature for 1 hour. Slides were washed twice, and DAB developing reagent (Vector Laboratories, Cat #SK-4105) was added to slides. Slides were dehydrated with increasing concentrations of ethanol and cleared using xylene. Slides were cover-slipped, dried, and imaged using brightfield setting on EVOS M5000 inverted microscope.

RNA Sequencing

RNA was isolated from tissues as previously described above. 500ng-1μg of total RNA per sample was enriched for polyadenylated RNA and prepared for RNA sequencing using the TruSeq Stranded mRNA Library Prep Kit (Illumina) per manufacturer instructions. Samples were sequenced on an Illumina NextSeq 500 platform or by the NYU Langone Genome Technology Center. FASTQ files were then aligned to the golden hamster genome (MesAur 1.0, ensembl) via the RNA-Seq Alignment application (BaseSpace, Illumina). Salmon files were analyzed using DESeq2 (125). For non-ontology analyses, all genes with an adjusted *P*-value (*P*-adj) less than 0.1 were considered DEGs.

Ontological analysis was performed using g:Profiler and Qiagen Ingenuity Pathway Analysis, targeting genes with a nominal p-value of less than 0.05 to increase analytical power. All visualizations of RNA-seq, differential expression analysis, and ontological analysis data were created by the respective ontological analysis programs or by R using ggplot2, VennDiagram, Circos, pheatmap, ComplexHeatmap, and gplots packages.

Gene set enrichment analyses were conducted using the GSEA Java application for Mac (v 4.1.0) (MSigDB; Broad Institute, UC San Diego). Analyses were performed on pre-ranked gene lists derived from differential expression data. Genes were ranked by the following statistic: -log10(p-value)/sign(log2FoldChange). GSEA analyses were conducted against the C8 cell type signature gene set (v7.4) provided by the Molecular Signatures Database (MSigDB).

Cell Subtype Deconvolution

Gene read counts from alignments were processed using the Multi-subject Single-cell Deconvolution (MuSiC) program's "music_prop" function (126). Annotated gene count matrices derived from single-nucleus RNA-sequencing of DRG tissues in the Renthal *et al.* study were used as a reference (127). This dataset included use of all available single cell data from non-transgenic C57 background animals in NCBI GEO accession dataset GSE154659. MuSiC output for proportional representation of cell subtypes was compared amongst sample groups using an f-test followed by an unpaired t-test. As reference datasets were generated from murine tissues, hamster gene names were substituted for murine ortholog gene using Ensembl BioMart where available. When murine orthologs were unavailable, human ortholog, and then hamster gene names were used.

Meta-Analysis

FASTQ files from Parisien *et al.* (2019) (97) generated from RNA-seq of DRG tissues from mice subjected to sham (mock), CFA, and SNI treatments were obtained from NCBI GEO (GSE111216). Paired end read files were aligned to the *Mus musculus* transcriptome (GRCm39) and quantified using Salmon (version 1.4.0). Salmon files were analyzed for differentially expressed genes using DESeq2, and all genes expressing a *P*-adj. < 0.1 were considered differentially expressed. Differentially expressed genes from murine DRG injury models compared to mock tissues were compared to analogous differentially expressed genes from infected hamster DRG tissues compared to mock hamster DRG tissues. These comparative analyses were visualized using Circos, VennDiagram, and ggplot2. Shared and

contra-regulated gene sets highlighted from these analyses were also analyzed for ontology using g:Profiler.

Statistical Analyses

All statistical analyses outside of sequencing-related assays were performed in GraphPad Prism Version 10. Repeated measure one- and two-way ANOVAs were used to compare the effects of virus type and time of infection on mechanical hypersensitivity, and post-hoc Tukey's multiple comparison test were used to perform timepoint comparisons for the Von Frey assay. Multiple t-tests and two-way ANOVAs were used for qPCR analysis and RNA-seq deconvolution.

RNA-seq data was analyzed as described above. Ontology analysis statistics were performed with either Ingenuity Pathway Analysis (IPA), g:Profiler, or Enrichr (128).

Supplementary Material

Refer to Web version on PubMed Central for supplementary material.

ACKNOWLEDGEMENTS

DATA AND MATERIALS AVAILABILITY

RNA-seq data have been deposited to NCBI GEO (accession ID GSE224710). All data needed to evaluate the conclusions in the paper are present in the paper or the Supplementary Materials.

References and Notes

1. Pascarella G, Strumia A, Piliego C, Bruno F, Del Buono R, Costa F, Scarlata S, Agrò FE, COVID-19 diagnosis and management: a comprehensive review. J. Intern. Med. 288 (2020), doi:10.1111/joim.13091.

2. Caronna E, Ballvé A, Llauradó A, Gallardo VJ, María Ariton D, Lallana S, Maza SL, Gadea MO, Quibus L, Restrepo JL, Rodrigo-Gisbert M, Vilaseca A, Gonzalez MH, Gallo MM, Alpuente A, Torres-Ferrus M, Borrell RP, Alvarez-Sabin J, Pozo-Rosich P, Headache: A striking prodromal and persistent symptom, predictive of COVID-19 clinical evolution. Cephalalgia 40 (2020), doi:10.1177/0333102420965157.

3. Amanat M, Rezaei N, Roozbeh M, Shojaei M, Tafakhori A, Zoghi A, Darazam IA, Salehi M, Karimialavijeh E, Lima BS, Garakani A, Vaccaro A, Ramezani M, Neurological manifestations as the predictors of severity and mortality in hospitalized individuals with COVID-19: a multicenter prospective clinical study. BMC Neurol. 21 (2021), doi:10.1186/s12883-021-02152-5.

4. Escalard S, Chalumeau V, Escalard C, Redjem H, Delvoye F, Hébert S, Smajda S, Ciccio G, Desilles JP, Mazighi M, Blanc R, Maïer B, Piotin M, Early brain imaging shows increased severity of acute

ischemic strokes with large vessel occlusion in COVID-19 patients. Stroke (2020), doi:10.1161/STROKEAHA.120.031011.

5. Halushka MK, Vander Heide RS, Myocarditis is rare in COVID-19 autopsies: cardiovascular findings across 277 postmortem examinations. Cardiovasc. Pathol. 50 (2021), doi:10.1016/j.carpath.2020.107300.

6. Stevens JS, King KL, Robbins-Juarez SY, Khairallah P, Toma K, Verduzco HA, Daniel E, Douglas D, Moses AA, Peleg Y, Starakiewicz P, Li MT, Kim DW, Yu K, Qian L, Shah VH, O'Donnell MR, Cummings MJ, Zucker J, Natarajan K, Perotte A, Tsapepas D, Krzysztof K, Dube G, Siddall E, Shirazian S, Nickolas TL, Rao MK, Barasch JM, Valeri AM, Radhakrishnan J, Gharavi AG, Husain SA, Mohan S, High rate of renal recovery in survivors of COVID-19 associated acute renal failure requiring renal replacement therapy. PLoS One 15 (2020), doi:10.1371/journal.pone.0244131.

7. Song XJ, Xiong DL, Wang ZY, Yang D, Zhou L, Li RC, Pain Management during the COVID-19 Pandemic in China: Lessons Learned. Pain Med. (United States) (2020), doi:10.1093/PM/PNAA143.

8. Ellul MA, Benjamin L, Singh B, Lant S, Michael BD, Easton A, Kneen R, Defres S, Sejvar J, Solomon T, Neurological associations of COVID-19. Lancet Neurol. (2020), doi:10.1016/S1474-4422(20)30221-0.

9. Andalib S, Biller J, Di Napoli M, Moghimi N, McCullough LD, Rubinos CA, O'Hana Nobleza C, Azarpazhooh MR, Catanese L, Elicer I, Jafari M, Liberati F, Camejo C, Torbey M, Divani AA, Peripheral Nervous System Manifestations Associated with COVID-19. Curr. Neurol. Neurosci. Rep. (2021), doi:10.1007/s11910-021-01102-5.

10. Carfì A, Bernabei R, Landi F, Persistent symptoms in patients after acute COVID-19. J. Am. Med. Assoc. 324 (2020), doi:10.1001/jama.2020.12603.

11. Stavem K, Ghanima W, Olsen MK, Gilboe HM, Einvik G, Persistent symptoms 1.5–6 months after COVID-19 in non-hospitalised subjects: A population-based cohort study. Thorax 76 (2021), doi:10.1136/thoraxjnl-2020-216377.

12. A clinical case definition of post COVID-19 condition by a Delphi consensus, 6 October 2021. World Heal. Organ. (2021).

13. Sudre CH, Murray B, Varsavsky T, Graham MS, Penfold RS, Bowyer RC, Pujol JC, Klaser K, Antonelli M, Canas LS, Molteni E, Modat M, Jorge Cardoso M, May A, Ganesh S, Davies R, Nguyen LH, Drew DA, Astley CM, Joshi AD, Merino J, Tsereteli N, Fall T, Gomez MF, Duncan EL, Menni C, Williams FMK, Franks PW, Chan AT, Wolf J, Ourselin S, Spector T, Steves CJ, Attributes and predictors of long COVID. Nat. Med. (2021), doi:10.1038/s41591-021-01292-y.

14. Davis HE, Assaf GS, McCorkell L, Wei H, Low RJ, Re'em Y, Redfield S, Austin JP, Akrami A, Characterizing long COVID in an international cohort: 7 months of symptoms and their impact. EClinicalMedicine (2021), doi:10.1016/j.eclinm.2021.101019.

15. Sigfrid L, Drake TM, Pauley E, Jesudason EC, Olliaro P, Lim WS, Gillesen A, Berry C, Lowe DJ, McPeake J, Lone N, Munblit D, Casey A, Bannister P, Russell CD, Goodwin L, Ho A, Turtle L, O'Hara ME, Hastie C, Donohue C, Spencer RG, Donegan C, Gummery A, Harrison J, Hardwick HE, Hastie CE, Carson G, Merson L, Baillie JK, Openshaw P, Harrison EM, Docherty AB, Semple MG, Scott JT, Long Covid in adults discharged from UK hospitals after Covid-19: A prospective, multicentre cohort study using the ISARIC WHO Clinical Characterisation Protocol. Lancet Reg. Heal. - Eur. (2021), doi:10.1016/j.lanepe.2021.100186.

16. Zhao HJ, Lu XX, Bin Deng Y, Tang YJ, Lu JC, COVID-19: Asymptomatic carrier transmission is an underestimated problem. Epidemiol. Infect. (2020), doi:10.1017/S0950268820001235.

17. Gao Z, Xu Y, Sun C, Wang X, Guo Y, Qiu S, Ma K, A systematic review of asymptomatic infections with COVID-19. J. Microbiol. Immunol. Infect. (2021), doi:10.1016/j.jmii.2020.05.001.

18. Rowbotham MC, Petersen KL, Zoster-associated pain and neural dysfunction. Pain (2001), doi:10.1016/S0304-3959(01)00328-1.

19. Verma S, Estanislao L, Simpson D, HIV-associated neuropathic pain: Epidemiology, pathophysiology and management. CNS Drugs 19, 325–334 (2005). [PubMed: 15813646]

20. Wu Y, Xu X, Chen Z, Duan J, Hashimoto K, Yang L, Liu C, Yang C, Nervous system involvement after infection with COVID-19 and other coronaviruses. Brain. Behav. Immun. (2020), doi:10.1016/j.bbi.2020.03.031.

21. Huang L, Ou R, Rabelo de Souza G, Cunha TM, Lemos H, Mohamed E, Li L, Pacholczyk G, Randall J, Munn DH, Mellor AL, Virus Infections Incite Pain Hypersensitivity by Inducing Indoleamine 2,3 Dioxygenase. PLoS Pathog. 12 (2016), doi:10.1371/journal.ppat.1005615.

22. Kaji M, Watanabe A, Aizawa H, Differences in clinical features between influenza A H1N1, A H3N2, and B in adult patients. Respirology 8 (2003), doi:10.1046/j.1440-1843.2003.00457.x.

23. Garry EM, Delaney A, Anderson HA, Sirinathsinghji EC, Clapp RH, Martin WJ, Kinchington PR, Krah DL, Abbadie C, Fleetwood-Walker SM, Varicella zoster virus induces neuropathic changes in rat dorsal root ganglia and behavioral reflex sensitisation that is attenuated by gabapentin or sodium channel blocking drugs. Pain (2005), doi:10.1016/j.pain.2005.08.003.

24. Takasaki I, Andoh T, Shiraki K, Kuraishi Y, Allodynia and hyperalgesia induced by herpes simplex virus type-1 infection in mice. Pain (2000), doi:10.1016/S0304-3959(00)00240-2.

25. Pardo CA, McArthur JC, Griffin JW, in Journal of the Peripheral Nervous System, (2001).

26. Maratou K, Wallace VCJ, Hasnie FS, Okuse K, Hosseini R, Jina N, Blackbeard J, Pheby T, Orengo C, Dickenson AH, McMahon SB, Rice ASC, Comparison of dorsal root ganglion gene expression in rat models of traumatic and HIV-associated neuropathic pain. Eur. J. Pain (2009), doi:10.1016/j.ejpain.2008.05.011.

27. Oaklander AL, Clinical significance of angiotensin-converting enzyme 2 receptors for severe acute respiratory syndrome coronavirus 2 (COVID-19) on peripheral small-fiber sensory neurons is unknown today. Pain (2020), doi:10.1097/j.pain.0000000000002050.

28. Paniz-Mondolfi A, Bryce C, Grimes Z, Gordon RE, Reidy J, Lednicky J, Sordillo EM, Fowkes M, Central nervous system involvement by severe acute respiratory syndrome coronavirus-2 (SARS-CoV-2). J. Med. Virol. (2020), doi:10.1002/jmv.25915.

29. Matschke J, Lütgehetmann M, Hagel C, Sperhake JP, Schröder AS, Edler C, Mushumba H, Fitzek A, Allweiss L, Dandri M, Dottermusch M, Heinemann A, Pfefferle S, Schwabenland M, Sumner Magruder D, Bonn S, Prinz M, Gerloff C, Püschel K, Krasemann S, Aepfelbacher M, Glatzel M, Neuropathology of patients with COVID-19 in Germany: a post-mortem case series. Lancet Neurol. 19 (2020), doi:10.1016/S1474-4422(20)30308-2.

30. Schurink B, Roos E, Radonic T, Barbe E, Bouman CSC, de Boer HH, de Bree GJ, Bulle EB, Aronica EM, Florquin S, Fronczek J, Heunks LMA, de Jong MD, Guo L, du Long R, Lutter R, Molenaar PCG, Neefjes-Borst EA, Niessen HWM, van Noesel CJM, Roelofs JJTH, Snijder EJ, Soer EC, Verheij J, Vlaar APJ, Vos W, van der Wel NN, van der Wal AC, van der Valk P, Bugiani M, Viral presence and immunopathology in patients with lethal COVID-19: a prospective autopsy cohort study. The Lancet Microbe 1 (2020), doi:10.1016/S2666-5247(20)30144-0.

31. Thakur KT, Miller EH, Glendinning MD, Al-Dalahmah O, Banu MA, Boehme AK, Boubour AL, Bruce SS, Chong AM, Claassen J, Faust PL, Hargus G, Hickman RA, Jambawalikar S, Khandji AG, Kim CY, Klein RS, Lignelli-Dipple A, Lin CC, Liu Y, Miller ML, Moonis G, Nordvig AS, Overdevest JB, Prust ML, Przedborski S, Roth WH, Soung A, Tanji K, Teich AF, Agalliu D, Uhlemann AC, Goldman JE, Canoll P, COVID-19 neuropathology at Columbia University Irving Medical Center/New York Presbyterian Hospital. Brain 144 (2021), doi:10.1093/brain/awab148.

32. Menter T, Haslbauer JD, Nienhold R, Savic S, Hopfer H, Deigendesch N, Frank S, Turek D, Willi N, Pargger H, Bassetti S, Leuppi JD, Cathomas G, Tolnay M, Mertz KD, Tzankov A, Postmortem examination of COVID-19 patients reveals diffuse alveolar damage with severe capillary congestion and variegated findings in lungs and other organs suggesting vascular dysfunction. Histopathology 77 (2020), doi:10.1111/his.14134.

33. Hoagland DA, Møller R, Uhl SA, Oishi K, Frere J, Golynker I, Horiuchi S, Panis M, Blanco-Melo D, Sachs D, Arkun K, Lim JK, tenOever BR, Leveraging the antiviral type I interferon system as a first line of defense against SARS-CoV-2 pathogenicity. Immunity 54 (2021), doi:10.1016/j.immuni.2021.01.017.

34. Frere JJ, Serafini RA, Pryce KD, Zazhytska M, Oishi K, Golynker I, Panis M, Zimering J, Horiuchi S, Hoagland DA, Møller R, Ruiz A, Kodra A, Overdevest JB, Canoll PD, Borczuk AC, Chandar V, Bram Y, Schwartz R, Lomvardas S, Zachariou V, tenOever BR, SARS-CoV-2 infection in hamsters and humans results in lasting and unique systemic perturbations post recovery. Sci. Transl. Med. (2022) doi: 10.1126/scitranslmed.abq3059.

35. Zanin L, Saraceno G, Panciani PP, Renisi G, Signorini L, Migliorati K, Fontanella MM, SARS-CoV-2 can induce brain and spine demyelinating lesions. Acta Neurochir. (Wien). (2020), doi:10.1007/s00701-020-04374-x.

36. Aragão MFVV, Leal MC, Cartaxo Filho OQ, Fonseca TM, Valença MM, Anosmia in COVID-19 associated with injury to the olfactory bulbs evident on MRI. Am. J. Neuroradiol. (2020), doi:10.3174/ajnr.A6675.

37. Roy-Gash F, Marine DM, Jean-Michel D, Herve V, Raphael B, Nicolas E, COVID-19-associated acute cerebral venous thrombosis: Clinical, CT, MRI and EEG features. Crit. Care (2020), doi:10.1186/s13054-020-03131-x.

38. Carroll E, Lewis A, Catastrophic Intracranial Hemorrhage in Two Critically Ill Patients with COVID-19. Neurocrit. Care (2020), doi:10.1007/s12028-020-00993-5.

39. Fernandez CE, Franz CK, Ko JH, Walter JM, Koralnik IJ, Ahlawat S, Deshmukh S, Imaging review of peripheral nerve injuries in patients with COVID-19. Radiology (2021), doi:10.1148/radiol.2020203116.

40. Abrams RMC, Simpson DM, Navis A, Jette N, Zhou L, Shin SC, Small fiber neuropathy associated with SARS-CoV-2 infection. Muscle and Nerve (2021), doi:10.1002/mus.27458.

41. Neumann B, Schmidbauer ML, Dimitriadis K, Otto S, Knier B, Niesen WD, Hosp JA, Günther A, Lindemann S, Nagy G, Steinberg T, Linker RA, Hemmer B, Bösel J, Cerebrospinal fluid findings in COVID-19 patients with neurological symptoms. J. Neurol. Sci. (2020), doi:10.1016/j.jns.2020.117090.

42. Destras G, Bal A, Escuret V, Morfin F, Lina B, Josset L, Systematic SARS-CoV-2 screening in cerebrospinal fluid during the COVID-19 pandemic. The Lancet Microbe (2020), doi:10.1016/S2666-5247(20)30066-5.

43. Huang YH, Jiang D, Huang JT, SARS-CoV-2 Detected in Cerebrospinal Fluid by PCR in a Case of COVID-19 Encephalitis. Brain. Behav. Immun. (2020), doi:10.1016/j.bbi.2020.05.012.

44. Domingues RB, Mendes-Correa MC, de Moura Leite FBV, Sabino EC, Salarini DZ, Claro I, Santos DW, de Jesus JG, Ferreira NE, Romano CM, Soares CAS, First case of SARS-COV-2 sequencing in cerebrospinal fluid of a patient with suspected demyelinating disease. J. Neurol. (2020), doi:10.1007/s00415-020-09996-w.

45. Li YC, Bai WZ, Hirano N, Hayashida T, Hashikawa T, Coronavirus infection of rat dorsal root ganglia: Ultrastructural characterization of viral replication, transfer, and the early response of satellite cells. Virus Res. (2012), doi:10.1016/j.virusres.2011.12.021.

46. Perlman S, Jacobsen G, Olson AL, Afifi A, Identification of the spinal cord as a major site of persistence during during chronic infection with a murine coronavirus. Virology (1990), doi:10.1016/0042-6822(90)90426-R.

47. Elliott R, Li F, Dragomir I, Chua MMW, Gregory BD, Weiss SR, Analysis of the Host Transcriptome from Demyelinating Spinal Cord of Murine Coronavirus-Infected Mice. PLoS One (2013), doi:10.1371/journal.pone.0075346.

48. Koyuncu OO, Hogue IB, Enquist LW, Virus infections in the nervous system. Cell Host Microbe (2013), doi:10.1016/j.chom.2013.03.010.

49. Hosseini S, Wilk E, Michaelsen-Preusse K, Gerhauser I, Baumgärtner W, Geffers R, Schughart K, Korte M, Long-term neuroinflammation induced by influenza a virus infection and the impact on hippocampal neuron morphology and function. J. Neurosci. (2018), doi:10.1523/JNEUROSCI.1740-17.2018.

50. Dobrindt K, Hoagland DA, Seah C, Kassim B, O'Shea CP, Murphy A, Iskhakova M, Fernando MB, Powell SK, Deans PJM, Javidfar B, Peter C, Møller R, Uhl SA, Garcia MF, Kimura M, Iwasawa K, Crary JF, Kotton DN, Takebe T, Huckins LM, tenOever BR, Akbarian S, Brennand KJ, Common Genetic Variation in Humans Impacts In Vitro Susceptibility to SARS-CoV-2 Infection. Stem Cell Reports 16 (2021), doi:10.1016/j.stemcr.2021.02.010.

51. Song E, Zhang C, Israelow B, Lu-Culligan A, Prado AV, Skriabine S, Lu P, El Weizman O, Liu F, Dai Y, Szigeti-Buck K, Yasumoto Y, Wang G, Castaldi C, Heltke J, Ng E, Wheeler J, Alfajaro MM, Levavasseur E, Fontes B, Ravindra NG, van Dijk D, Mane S, Gunel M, Ring A, Jaffar Kazmi SA, Zhang K, Wilen CB, Horvath TL, Plu I, Haik S, Thomas JL, Louvi A, Farhadian SF, Huttner

A, Seilhean D, Renier N, Bilguvar K, Iwasaki A, Neuroinvasion of SARS-CoV-2 in human and mouse brain. J. Exp. Med. 218 (2021), doi:10.1084/JEM.20202135.

52. Yang L, Han Y, Nilsson-Payant BE, Gupta V, Wang P, Duan X, Tang X, Zhu J, Zhao Z, Jaffré F, Zhang T, Kim TW, Harschnitz O, Redmond D, Houghton S, Liu C, Naji A, Ciceri G, Guttikonda S, Bram Y, Nguyen DHT, Cioffi M, Chandar V, Hoagland DA, Huang Y, Xiang J, Wang H, Lyden D, Borczuk A, Chen HJ, Studer L, Pan FC, Ho DD, tenOever BR, Evans T, Schwartz RE, Chen S, A Human Pluripotent Stem Cell-based Platform to Study SARS-CoV-2 Tropism and Model Virus Infection in Human Cells and Organoids. Cell Stem Cell 27 (2020), doi:10.1016/j.stem.2020.06.015.

53. Sia SF, Yan LM, Chin AWH, Fung K, Choy KT, Wong AYL, Kaewpreedee P, Perera RAPM, Poon LLM, Nicholls JM, Peiris M, Yen HL, Pathogenesis and transmission of SARS-CoV-2 in golden hamsters. Nature 583 (2020), doi:10.1038/s41586-020-2342-5.

54. Morales DJ, Lenschow DJ, The antiviral activities of ISG15. J. Mol. Biol. 425 (2013), doi:10.1016/j.jmb.2013.09.041.

55. Barragán-Iglesias P, Franco-Enzástiga Ú, Jeevakumar V, Shiers S, Wangzhou A, Granados-Soto V, Campbell ZT, Dussor G, Price TJ, Type I interferons act directly on nociceptors to produce pain sensitization: Implications for viral infection-induced pain. J. Neurosci. 40 (2020), doi:10.1523/JNEUROSCI.3055-19.2020.

56. Eccles R, Understanding the symptoms of the common cold and influenza. Lancet Infect. Dis. (2005), doi:10.1016/S1473-3099(05)70270-X.

57. Pietzner M, Wheeler E, Carrasco-Zanini J, Raffler J, Kerrison ND, Oerton E, Auyeung VPW, Luan J, Finan C, Casas JP, Ostroff R, Williams SA, Kastenmüller G, Ralser M, Gamazon ER, Wareham NJ, Hingorani AD, Langenberg C, Genetic architecture of host proteins involved in SARS-CoV-2 infection. Nat. Commun. 11 (2020), doi:10.1038/s41467-020-19996-z.

58. Sharma A, Pollett MA, Plant GW, Harvey AR, Changes in mRNA expression of class 3 semaphorins and their receptors in the adult rat retino-collicular system after unilateral optic nerve injury. Investig. Ophthalmol. Vis. Sci. (2012), doi:10.1167/iovs.12-10799.

59. Verheyen A, Peeraer E, Nuydens R, Dhondt J, Poesen K, Pintelon I, Daniels A, Timmermans JP, Meert T, Carmeliet P, Lambrechts D, Systemic anti-vascular endothelial growth factor therapies induce a painful sensory neuropathy. Brain (2012), doi:10.1093/brain/aws145.

60. Moutal A, Martin LF, Boinon L, Gomez K, Ran D, Zhou Y, Stratton HJ, Cai S, Luo S, Gonzalez KB, Perez-Miller S, Patwardhan A, Ibrahim MM, Khanna R, SARS-CoV-2 spike protein co-opts VEGF-A/neuropilin-1 receptor signaling to induce analgesia. Pain (2021), doi:10.1097/j.pain.0000000000002097.

61. Taccola G, Doyen PJ, Damblon J, Dingu N, Ballarin B, Steyaert A, des Rieux A, Forget P, Hermans E, Bosier B, Deumens R, A new model of nerve injury in the rat reveals a role of Regulator of G protein Signaling 4 in tactile hypersensitivity. Exp. Neurol. (2016), doi:10.1016/j.expneurol.2016.09.008.

62. Prasad K, Khatoon F, Rashid S, Ali N, AlAsmari AF, Ahmed MZ, Alqahtani AS, Alqahtani MS, Kumar V, Targeting hub genes and pathways of innate immune response in COVID-19: A network biology perspective. Int. J. Biol. Macromol. (2020), doi:10.1016/j.ijbiomac.2020.06.228.

63. Provenzi L, Fumagalli M, Scotto di Minico G, Giorda R, Morandi F, Sirgiovanni I, Schiavolin P, Mosca F, Borgatti R, Montirosso R, Pain-related increase in serotonin transporter gene methylation associates with emotional regulation in 4.5-year-old preterm-born children. Acta Paediatr. Int. J. Paediatr. (2020), doi:10.1111/apa.15077.

64. Raju HB, Tsinoremas NF, Capobianco E, Emerging putative associations between non-coding RNAs and protein-coding genes in neuropathic pain: Added value from reusing microarray data. Front. Neurol. (2016), doi:10.3389/fneur.2016.00168.

65. Li X, Wang W, Chen Q, Zhou Y, Wang L, Huang H, Antinociceptive effects of IL-6R vs. glucocorticoid receptors during rat hind paw inflammatory pain. Neurosci. Lett. (2020), doi:10.1016/j.neulet.2020.135356.

66. Zhang D, Mou JY, Wang F, Liu J, Hu X, CRNDE enhances neuropathic pain via modulating miR-136/IL6R axis in CCI rat models. J. Cell. Physiol. (2019), doi:10.1002/jcp.28790.

67. Wakabayashi H, Kato S, Nagao N, Miyamura G, Naito Y, Sudo A, Interleukin-6 Inhibitor Suppresses Hyperalgesia Without Improvement in Osteoporosis in a Mouse Pain Model of Osteoporosis. Calcif. Tissue Int. (2019), doi:10.1007/s00223-019-00521-4.

68. Ji RR, Baba H, Brenner GJ, Woolf CJ, Nociceptive-specific activation of ERK in spinal neurons contributes to pain hypersensitivity. Nat. Neurosci. (1999), doi:10.1038/16040.

69. Ciruela A, Dixon AK, Bramwell S, Gonzalez MI, Pinnock RD, Lee K, Identification of MEK1 as a novel target for the treatment of neuropathic pain. Br. J. Pharmacol. (2003), doi:10.1038/sj.bjp.0705103.

70. Yamakita S, Horii Y, Takemura H, Matsuoka Y, Yamashita A, Yamaguchi Y, Matsuda M, Sawa T, Amaya F, Synergistic activation of ERK1/2 between A-fiber neurons and glial cells in the DRG contributes to pain hypersensitivity after tissue injury. Mol. Pain (2018), doi:10.1177/1744806918767508.

71. Zhang J, Jiang J, Bao G, Xu G, Wang L, Chen J, Chen C, Wu C, Xue P, Xu D, Sun Y, Cui Z, Interaction between C/EBPβ and RUNX2 promotes apoptosis of chondrocytes during human lumbar facet joint degeneration. J. Mol. Histol. (2020), doi:10.1007/s10735-020-09891-8.

72. Rice SJ, Aubourg G, Sorial AK, Almarza D, Tselepi M, Deehan DJ, Reynard LN, Loughlin J, Identification of a novel, methylation-dependent, RUNX2 regulatory region associated with osteoarthritis risk. Hum. Mol. Genet. (2018), doi:10.1093/hmg/ddy257.

73. Tajar A, McBeth J, Lee DM, MacFarlane GJ, Huhtaniemi IT, Finn JD, Bartfai G, Boonen S, Casanueva FF, Forti G, Giwercman A, Han TS, Kula K, Labrie F, Lean MEJ, Pendleton N, Punab M, Silman AJ, Vanderschueren D, O'Neill TW, Wu FCW, Elevated levels of gonadotrophins but not sex steroids are associated with musculoskeletal pain in middle-aged and older European men. Pain (2011), doi:10.1016/j.pain.2011.01.048.

74. Xie MX, Cao XY, Zeng WA, Lai RC, Guo L, Wang JC, Bin Xiao Y, Zhang X, Chen D, Liu XG, Zhang XL, ATF4 selectively regulates heat nociception and contributes to kinesin-mediated TRPM3 trafficking. Nat. Commun. (2021), doi:10.1038/s41467-021-21731-1.

75. Dong L, Guarino BB, Jordan-Sciutto KL, Winkelstein BA, Activating transcription factor 4, a mediator of the integrated stress response, is increased in the dorsal root ganglia following painful facet joint distraction. Neuroscience (2011), doi:10.1016/j.neuroscience.2011.07.059.

76. Russe OQ, Möser CV, Kynast KL, King TS, Stephan H, Geisslinger G, Niederberger E, Activation of the AMP-activated protein kinase reduces inflammatory nociception. J. Pain (2013), doi:10.1016/j.jpain.2013.05.012.

77. King-Himmelreich TS, Möser CV, Wolters MC, Schmetzer J, Schreiber Y, Ferreirós N, Russe OQ, Geisslinger G, Niederberger E, AMPK contributes to aerobic exercise-induced antinociception downstream of endocannabinoids. Neuropharmacology (2017), doi:10.1016/j.neuropharm.2017.05.002.

78. Giaccone G, Zatloukal P, Roubec J, Floor K, Musil J, Kuta M, Van Klaveren RJ, Chaudhary S, Gunther A, Shamsili S, Multicenter phase II trial of YM155, a small-molecule suppressor of survivin, in patients with advanced, refractory, non-small-cell lung cancer. J. Clin. Oncol. (2009), doi:10.1200/JCO.2008.21.1862.

79. Clemens MR, Gladkov OA, Gartner E, Vladimirov V, Crown J, Steinberg J, Jie F, Keating A, Phase II, multicenter, open-label, randomized study of YM155 plus docetaxel as first-line treatment in patients with HER2-negative metastatic breast cancer. Breast Cancer Res. Treat. (2015), doi:10.1007/s10549-014-3238-6.

80. Tolcher AW, Quinn DI, Ferrari A, Ahmann F, Giaccone G, Drake T, Keating A, De Bono JS, A phase II study of YM155, a novel small-molecule suppressor of survivin, in castration-resistant taxane-pretreated prostate cancer. Ann. Oncol. (2012), doi:10.1093/annonc/mdr353.

81. Yamauchi T, Nakamura N, Hiramoto M, Yuri M, Yokota H, Naitou M, Takeuchi M, Yamanaka K, Kita A, Nakahara T, Kinoyama I, Matsuhisa A, Kaneko N, Koutoku H, Sasamata M, Kobori M, Katou M, Tawara S, Kawabata S, Furuichi K, Sepantronium Bromide (YM155) induces disruption of the ILF3/p54nrb complex, which is required for survivin expression. Biochem. Biophys. Res. Commun. (2012), doi:10.1016/j.bbrc.2012.07.103.

82. Nakahara T, Takeuchi M, Kinoyama I, Minematsu T, Shirasuna K, Matsuhisa A, Kita A, Tominaga F, Yamanaka K, Kudoh M, Sasamata M, YM155, a novel small-molecule survivin suppressant,

induces regression of established human hormone-refractory prostate tumor xenografts. Cancer Res. (2007), doi:10.1158/0008-5472.CAN-07-1343.

83. Avrampou K, Pryce KD, Ramakrishnan A, Sakloth F, Gaspari S, Serafini RA, Mitsi V, Polizu C, Swartz C, Ligas B, Richards A, Shen L, Carr FB, Zachariou V, RGS4 Maintains Chronic Pain Symptoms in Rodent Models. J. Neurosci. 39, 8291–8304 (2019). [PubMed: 31308097]

84. Vachon-Presseau E, Tétreault P, Petre B, Huang L, Berger SE, Torbey S, Baria AT, Mansour AR, Hashmi JA, Griffith JW, Comasco E, Schnitzer TJ, Baliki MN, Apkarian AV, Corticolimbic anatomical characteristics predetermine risk for chronic pain. Brain 139, 1958–1970 (2016). [PubMed: 27190016]

85. Gómez K, Sandoval A, Barragán-Iglesias P, Granados-Soto V, Delgado-Lezama R, Felix R, González-Ramírez R, Transcription Factor Sp1 Regulates the Expression of Calcium Channel α2δ-1 Subunit in Neuropathic Pain. Neuroscience (2019), doi:10.1016/j.neuroscience.2019.06.011.

86. Li S, Zhao F, Tang Q, Xi C, He J, Wang Y, Zhu MX, Cao Z, Sarco/endoplasmic reticulum Ca 2+ -ATPase 2b mediates oxidation-induced endoplasmic reticulum stress to regulate neuropathic pain. Br. J. Pharmacol. (2021), doi:10.1111/bph.15744.

87. Kao DJ, Li AH, Chen JC, Luo RS, Chen YL, Lu JC, Wang HL, CC chemokine ligand 2 upregulates the current density and expression of TRPV1 channels and Nav1.8 sodium channels in dorsal root ganglion neurons. J. Neuroinflammation (2012), doi:10.1186/1742-2094-9-189.

88. Xie W, Tan ZY, Barbosa C, Strong JA, Cummins TR, Zhang JM, Upregulation of the sodium channel Na v β4 subunit and its contributions to mechanical hypersensitivity and neuronal hyperexcitability in a rat model of radicular pain induced by local dorsal root ganglion inflammation. Pain (2016), doi:10.1097/j.pain.0000000000000453.

89. Barbosa C, Tan ZY, Wang R, Xie W, Strong JA, Patel RR, Vasko MR, Zhang JM, Cummins TR, Navβ4 regulates fast resurgent sodium currents and excitability in sensory neurons. Mol. Pain (2015), doi:10.1186/s12990-015-0063-9.

90. Broyl A, Corthals SL, Jongen JLM, van der Holt B, Kuiper R, de Knegt Y, van Duin M, el Jarari L, Bertsch U, Lokhorst HM, Durie BG, Goldschmidt H, Sonneveld P, Mechanisms of peripheral neuropathy associated with bortezomib and vincristine in patients with newly diagnosed multiple myeloma: a prospective analysis of data from the HOVON-65/GMMG-HD4 trial. Lancet Oncol. (2010), doi:10.1016/S1470-2045(10)70206-0.

91. Munawar N, Oriowo MA, Masocha W, Antihyperalgesic activities of endocannabinoids in a mouse model of antiretroviral-Induced neuropathic pain. Front. Pharmacol. (2017), doi:10.3389/fphar.2017.00136.

92. Fu R, Tang Y, Li W, Ren Z, Li D, Zheng J, Zuo W, Chen X, Zuo QK, Tam KL, Zou Y, Bachmann T, Bekker A, Ye JH, Endocannabinoid signaling in the lateral habenula regulates pain and alcohol consumption. Transl. Psychiatry (2021), doi:10.1038/s41398-021-01337-3.

93. Hu Z, Deng N, Liu K, Zhou N, Sun Y, Zeng W, CNTF-STAT3-IL-6 Axis Mediates Neuroinflammatory Cascade across Schwann Cell-Neuron-Microglia. Cell Rep. (2020), doi:10.1016/j.celrep.2020.107657.

94. Chung HJ, Kim JD, Kim KH, Jeong NY, G protein-coupled receptor, family C, group 5 (GPRC5B) downregulation in spinal cord neurons is involved in neuropathic pain. Korean J. Anesthesiol. (2014), doi:10.4097/kjae.2014.66.3.230.

95. Ferrari LF, Bogen O, Alessandri-Haber N, Levine E, Gear RW, Levine JD, Transient decrease in nociceptor GRK2 expression produces long-term enhancement in inflammatory pain. Neuroscience (2012), doi:10.1016/j.neuroscience.2012.07.004.

96. Eijkelkamp N, Heijnen CJ, Willemen HLDM, Deumens R, Joosten EAJ, Kleibeuker W, Den Hartog IJM, Van Velthoven CTJ, Nijboer C, Nassar MA, Dorn GW, Wood JN, Kavelaars A, GRK2: A novel cell-specific regulator of severity and duration of inflammatory pain. J. Neurosci. (2010), doi:10.1523/JNEUROSCI.5752-09.2010.

97. Parisien M, Samoshkin A, Tansley SN, Piltonen MH, Martin LJ, El-Hachem N, Dagostino C, Allegri M, Mogil JS, Khoutorsky A, Diatchenko L, Genetic pathway analysis reveals a major role for extracellular matrix organization in inflammatory and neuropathic pain. Pain (2019), doi:10.1097/j.pain.0000000000001471.

98. Imai M, Iwatsuki-Horimoto K, Hatta M, Loeber S, Halfmann PJ, Nakajima N, Watanabe T, Ujie M, Takahashi K, Ito M, Yamada S, Fan S, Chiba S, Kuroda M, Guan L, Takada K, Armbrust T, Balogh A, Furusawa Y, Okuda M, Ueki H, Yasuhara A, Sakai-Tagawa Y, Lopes TJS, Kiso M, Yamayoshi S, Kinoshita N, Ohmagari N, Hattori SI, Takeda M, Mitsuya H, Krammer F, Suzuki T, Kawaoka Y, Syrian hamsters as a small animal model for SARS-CoV-2 infection and countermeasure development. Proc. Natl. Acad. Sci. U. S. A. 117 (2020), doi:10.1073/pnas.2009799117.

99. Muñoz-Fontela C, Dowling WE, Funnell SGP, Gsell PS, Riveros-Balta AX, Albrecht RA, Andersen H, Baric RS, Carroll MW, Cavaleri M, Qin C, Crozier I, Dallmeier K, de Waal L, de Wit E, Delang L, Dohm E, Duprex WP, Falzarano D, Finch CL, Frieman MB, Graham BS, Gralinski LE, Guilfoyle K, Haagmans BL, Hamilton GA, Hartman AL, Herfst S, Kaptein SJF, Klimstra WB, Knezevic I, Krause PR, Kuhn JH, Le Grand R, Lewis MG, Liu WC, Maisonnasse P, McElroy AK, Munster V, Oreshkova N, Rasmussen AL, Rocha-Pereira J, Rockx B, Rodríguez E, Rogers TF, Salguero FJ, Schotsaert M, Stittelaar KJ, Thibaut HJ, Te Tseng C, Vergara-Alert J, Beer M, Brasel T, Chan JFW, García-Sastre A, Neyts J, Perlman S, Reed DS, Richt JA, Roy CJ, Segalés J, Vasan SS, Henao-Restrepo AM, Barouch DH, Animal models for COVID-19. Nature 586 (2020), doi:10.1038/s41586-020-2787-6.

100. Gao G, Li W, Liu S, Han D, Yao X, Jin J, Han D, Sun W, Chen X, The positive feedback loop between ILF3 and lncrna ILF3-AS1 promotes melanoma proliferation, migration, and invasion. Cancer Manag. Res. (2018), doi:10.2147/CMAR.S186777.

101. Yang X, Lin F, Gao F, Up-regulated long non-coding RNA ILF3-AS1 indicates poor prognosis of nasopharyngeal carcinoma and promoted cell metastasis. Int. J. Biol. Markers (2020), doi:10.1177/1724600820955199.

102. hui Hu X, Dai J, lai Shang H, xue Zhao Z, dong Hao Y, SP1-mediated upregulation of lncRNA ILF3-AS1 functions a ceRNA for miR-212 to contribute to osteosarcoma progression via modulation of SOX5. Biochem. Biophys. Res. Commun. (2019), doi:10.1016/j.bbrc.2019.02.110.

103. Sanna MD, Galeotti N, The HDAC1/c-JUN complex is essential in the promotion of nerve injury-induced neuropathic pain through JNK signaling. Eur. J. Pharmacol. 825 (2018), doi:10.1016/j.ejphar.2018.02.034.

104. Sakloth F, Manouras L, Avrampou K, Mitsi V, Serafini RA, Pryce KD, Cogliani V, Berton O, Jarpe M, Zachariou V, HDAC6-selective inhibitors decrease nerve-injury and inflammation-associated mechanical hypersensitivity in mice. Psychopharmacology (Berl). 237 (2020), doi:10.1007/s00213-020-05525-9.

105. Shiers S, Mwirigi J, Pradhan G, Kume M, Black B, Barragan-Iglesias P, Moy JK, Dussor G, Pancrazio JJ, Kroener S, Price TJ, Reversal of peripheral nerve injury-induced neuropathic pain and cognitive dysfunction via genetic and tomivosertib targeting of MNK. Neuropsychopharmacology 45 (2020), doi:10.1038/s41386-019-0537-y.

106. Vasileiou I, Adamakis I, Patsouris E, Theocharis S, Ephrins and pain. Expert Opin. Ther. Targets (2013), doi:10.1517/14728222.2013.801456.

107. Hanamura K, Washburn HR, Sheffler-Collins SI, Xia NL, Henderson N, Tillu DV, Hassler S, Spellman DS, Zhang G, Neubert TA, Price TJ, Dalva MB, Extracellular phosphorylation of a receptor tyrosine kinase controls synaptic localization of NMDA receptors and regulates pathological pain. PLoS Biol. 15 (2017), doi:10.1371/journal.pbio.2002457.

108. Leroux A, Paiva dos Santos B, Leng J, Oliveira H, Amédée J, Sensory neurons from dorsal root ganglia regulate endothelial cell function in extracellular matrix remodelling. Cell Commun. Signal. (2020), doi:10.1186/s12964-020-00656-0.

109. Kerrisk ME, Cingolani LA, Koleske AJ, in Progress in Brain Research, (2014).

110. Knezevic NN, Yekkirala A, Yaksh TL, Basic/Translational Development of Forthcoming Opioid- and Nonopioid-Targeted Pain Therapeutics. Anesth. Analg. 125, 1714–1732 (2017). [PubMed: 29049116]

111. Yu X, Liu H, Hamel KA, Morvan MG, Yu S, Leff J, Guan Z, Braz JM, Basbaum AI, Dorsal root ganglion macrophages contribute to both the initiation and persistence of neuropathic pain. Nat. Commun. 11 (2020), doi:10.1038/s41467-019-13839-2.

112. Raoof R, Gil CM, Lafeber FPJG, De Visser H, Prado J, Versteeg S, Pascha MN, Heinemans ALP, Adolfs Y, Pasterkamp J, Wood JN, Mastbergen SC, Eijkelkamp N, Dorsal

root ganglia macrophages maintain osteoarthritis pain. J. Neurosci. 41 (2021), doi:10.1523/JNEUROSCI.1787-20.2021.

113. Huang ZZ, Li D, Liu CC, Cui Y, Zhu HQ, Zhang WW, Li YY, Xin WJ, CX3CL1-mediated macrophage activation contributed to paclitaxel-induced DRG neuronal apoptosis and painful peripheral neuropathy. Brain. Behav. Immun. 40 (2014), doi:10.1016/j.bbi.2014.03.014.

114. Wallace VCJ, Cottrell DF, Brophy PJ, Fleetwood-Walker SM, Focal lysolecithin-induced demyelination of peripheral afferents results in neuropathic pain behavior that is attenuated by cannabinoids. J. Neurosci. 23 (2003), doi:10.1523/jneurosci.23-08-03221.2003.

115. Yan W, Wu Z, Zhang Y, Hong D, Dong X, Liu L, Rao Y, Huang L, Zhang X, Wu J, The molecular and cellular insight into the toxicology of bortezomib-induced peripheral neuropathyBiomed. Pharmacother. 142 (2021), doi:10.1016/j.biopha.2021.112068.

116. Muglia P, Tozzi F, Galwey NW, Francks C, Upmanyu R, Kong XQ, Antoniades A, Domenici E, Perry J, Rothen S, Vandeleur CL, Mooser V, Waeber G, Vollenweider P, Preisig M, Lucae S, Müller-Myhsok B, Holsboer F, Middleton LT, Roses AD, Genome-wide association study of recurrent major depressive disorder in two European case-control cohorts. Mol. Psychiatry 15 (2010), doi:10.1038/mp.2008.131.

117. Wang Y, Li L, Xu C, Cao X, Liu Z, Sun N, Zhang A, Li X, Zhang K, Polymorphism of ERK/PTPRR Genes in Major Depressive Disorder at Resting-State Brain Function. Dev. Neuropsychol. 42 (2017), doi:10.1080/87565641.2017.1306527.

118. Muriello M, Kim AY, Sondergaard Schatz K, Beck N, Gunay-Aygun M, Hoover-Fong JE, Growth hormone deficiency, aortic dilation, and neurocognitive issues in Feingold syndrome 2. Am. J. Med. Genet. Part A 179 (2019), doi:10.1002/ajmg.a.61037.

119. Ganjavi H, Siu VM, Speevak M, MacDonald PA, A fourth case of Feingold syndrome type 2: Psychiatric presentation and management. BMJ Case Rep. 2014 (2014), doi:10.1136/bcr-2014-207501.

120. Wen Y, Fan X, Bu H, Ma L, Kong C, Huang C, Xu Y, Downregulation of lncRNA FIRRE relieved the neuropathic pain of female mice by suppressing HMGB1 expression. Mol. Cell. Biochem. 476 (2021), doi:10.1007/s11010-020-03949-7.

121. Hentsch L, Stancu P, Allali G, Lövblad KO, Lobrinus JA, Cocetta S, Pautex S, Uginet M, Serratrice J, Coen M, Decrease in pain perception during acute SARS-CoV-2 infection: a case series. Pain 163, 1019–1022 (2022). [PubMed: 34654780]

122. Fernández-De-las-Peñas C, de-La-Llave-Rincón AI, Ortega-Santiago R, Ambite-Quesada S, Gómez-Mayordomo V, Cuadrado ML, Arias-Navalón JA, Hernández-Barrera V, Martín-Guerrero JD, Pellicer-Valero OJ, Arendt-Nielsen L, Prevalence and risk factors of musculoskeletal pain symptoms as long-term post-COVID sequelae in hospitalized COVID-19 survivors: a multicenter study. Pain 163 (2022), doi:10.1097/j.pain.0000000000002564.

123. Oishi K, Horiuchi S, Minkoff JM, tenOever BR, The Host Response to In fl uenza A Virus Interferes with SARS-CoV-2 Replication during Coinfection. J. Virol. 96 (2022).

124. Pryce KD, Kang HJ, Sakloth F, Liu Y, Khan S, Toth K, Kapoor A, Nicolais A, Che T, Qin L, Bertherat F, Kaniskan HÜ, Jin J, Cameron MD, Roth BL, Zachariou V, Filizola M, A promising chemical series of positive allosteric modulators of the μ-opioid receptor that enhance the antinociceptive efficacy of opioids but not their adverse effects. Neuropharmacology 195 (2021), doi:10.1016/j.neuropharm.2021.108673.

125. Love MI, Huber W, Anders S, Moderated estimation of fold change and dispersion for RNA-seq data with DESeq2. Genome Biol. (2014), doi:10.1186/s13059-014-0550-8.

126. Wang X, Park J, Susztak K, Zhang NR, Li M, Bulk tissue cell type deconvolution with multi-subject single-cell expression reference. Nat. Commun. 10 (2019), doi:10.1038/s41467-018-08023-x.

127. Renthal W, Tochitsky I, Yang L, Cheng YC, Li E, Kawaguchi R, Geschwind DH, Woolf CJ, Transcriptional Reprogramming of Distinct Peripheral Sensory Neuron Subtypes after Axonal Injury. Neuron 108, 128–144.e9 (2020). [PubMed: 32810432]

128. Chen EY, Tan CM, Kou Y, Duan Q, Wang Z, Meirelles GV, Clark NR, Ma'ayan A, Enrichr: Interactive and collaborative HTML5 gene list enrichment analysis tool. BMC Bioinformatics (2013), doi:10.1186/1471-2105-14-128.
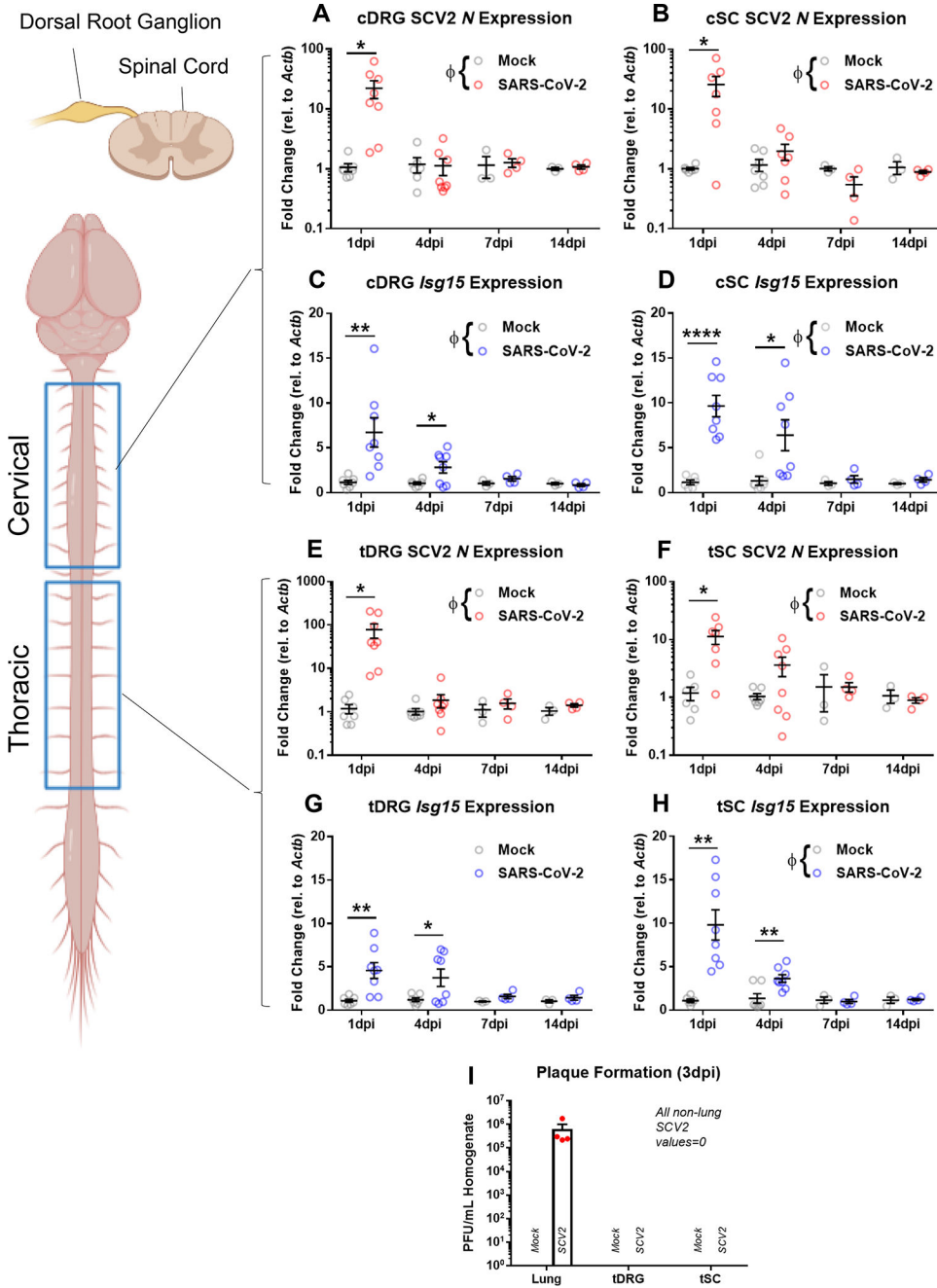
Figure 1. Viral mRNA and IFN-stimulated transcripts are acutely increased in the DRG and spinal cord by SARS-CoV-2.

(A and B) Expression of the nucleocapsid protein-encoding gene *N* in the cervical segment of DRGs and SC from male hamsters on the indicated days after infection (dpi) with SARS-CoV-2 or the mock control, as measured by qPCR. Data are mean ± SEM from n = 3–8 hamsters per group. $^{\Phi}P < 0.05$ by two-way ANOVA interaction factor; $^{*}P < 0.05$ and $^{**}P < 0.01$ by multiple t-tests. **(C and D)** Expression of IFN-stimulated gene 15 (*Isg15*) in cervical segments of DRGs and SCs, performed and analyzed as described in (A and B). $^{\Phi}P < 0.05$ by two-way ANOVA interaction factor; $^{*}P < 0.05$, $^{**}P < 0.01$, and $^{****}P$

< 0.0001 by multiple t-tests. **(E to H)** As described in (A to D), in thoracic segments of DRGs and spinal cords. **(I)** Plaque formation assay to detect the presence of mature virus in the lungs, thoracic DRGs, and thoracic spinal cords of mock- or SARS-CoV-2-infected male hamsters 3 days after infection (3 dpi). Data are mean ± SEM from n = 4 animals per group. Statistical analysis details for (A to H) are in table S2.
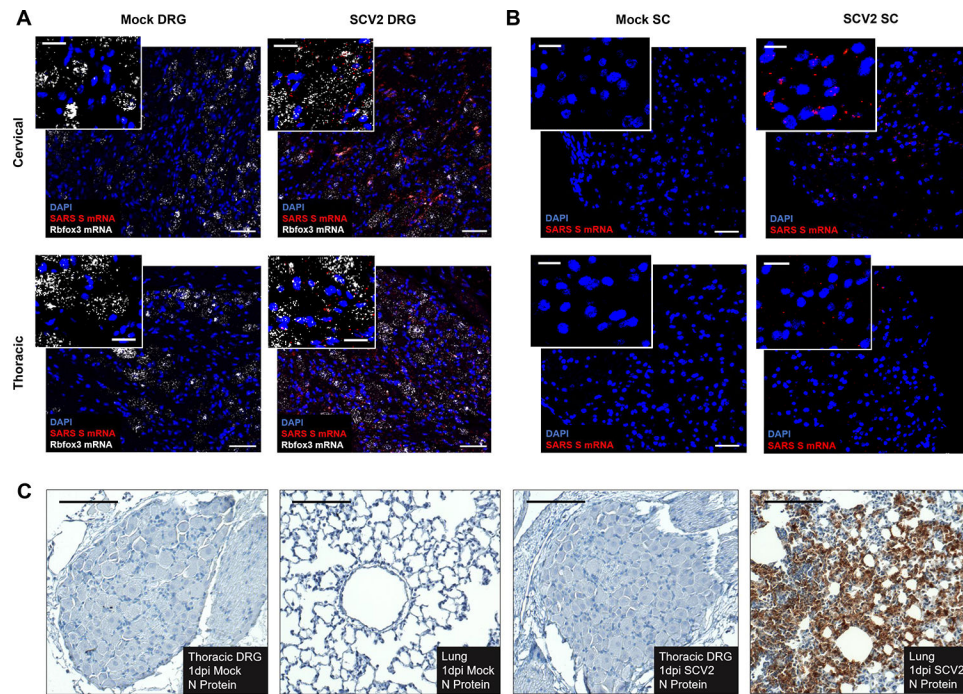
Figure 2. Viral mRNA is visibly detectable in DRG and SC by ISH, but mature virus is not detectable by IHC.

(A) Expression pattern of Spike RNA (red) around DAPI (blue) and *Rbfox3* (white) in cervical and thoracic DRGs of SARS-CoV-2-infected and mock male hamsters at 1 dpi. Data are representative of n = 2 animals per group. **(B)** Expression patterns of Spike RNA (red) around DAPI (blue) in cervical and thoracic SC from SARS-CoV-2-infected and mock-control male hamsters at 1 dpi. Data are representative of n = 2 per group. **(C)** Nucleocapsid protein expression pattern in thoracic DRGs of SARS-CoV-2-infected and mock-control male hamsters, as well as lung tissue of male SARS-CoV-2-infected animals at 1 dpi. Data is representative of n = 2 animals per group. Scale bars: 50 μm; insets, 20 μm.
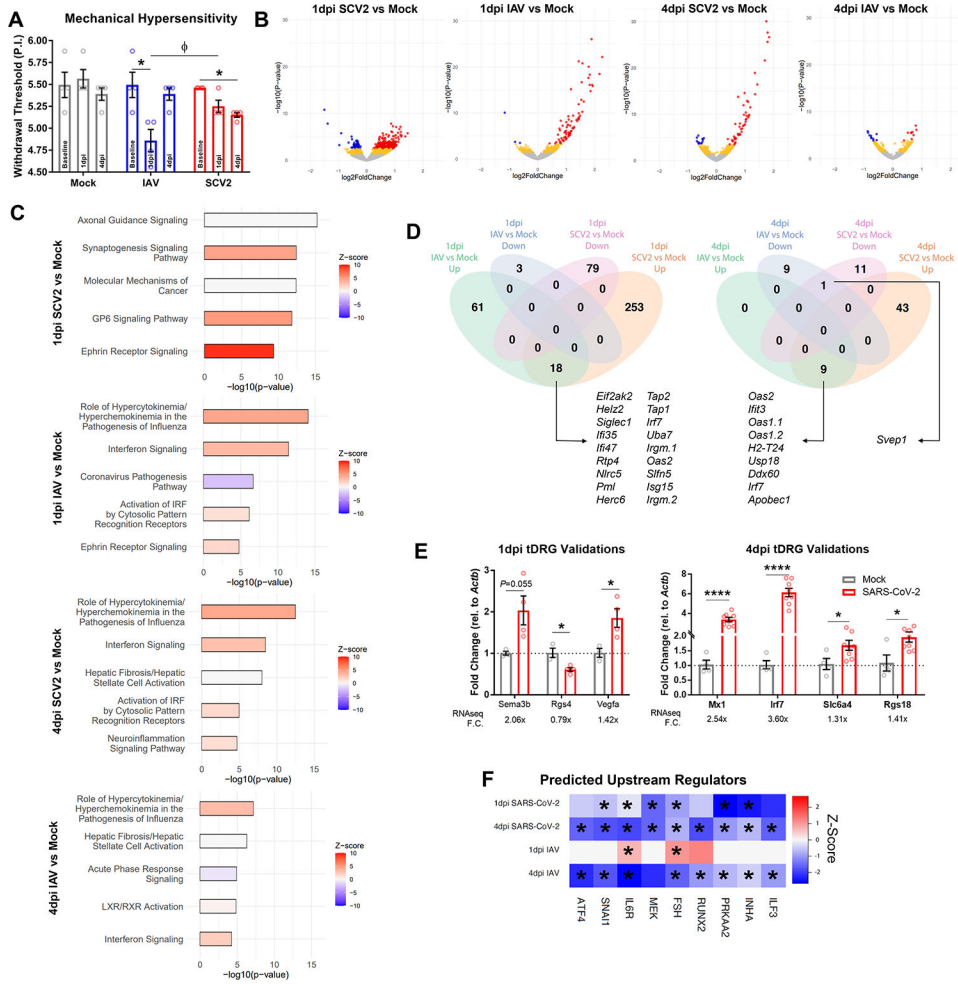
Figure 3. SARS-CoV-2 induces a unique behavioral phenotype and molecular signature in DRG tissue.

(**A**) Mechanical thresholds of mock-, IAV-, and SARS-CoV-2-infected male hamsters at baseline, 1 dpi, and 4 dpi. P.I. = linear perceived intensity. Data are expressed as mean ± SEM from n = 4 animals per group. *$P < 0.05$ by one-way ANOVA with Tukey's multiple comparisons (m.c.); $^{\Phi}$ $P < 0.05$ by two-way ANOVA Tukey's m.c., see also table S2. (**B**) Volcano plots of the RNA-seq data from tDRGs from SARS-CoV-2- or IAV-infected male hamsters at 1 and 4 dpi relative to mock-infected animals. Figure is representative of the combination of data from n = 4 animals per group. In (B): Red = P-adj. < 0.1, $\log_2 FC > 0$; blue = P-adj. < 0.1, $\log_2 FC < 0$; yellow = P-nom. < 0.05. (**C**) Top 5 IPA Canonical Pathways derived from the data described in (B); P-nom. < 0.05; -$\log_{10}$(p-value) > 1.3. (**D**) Petal diagrams derived from the RNA-seq data described in (B); P-adj. < 0.01, to identify commonly upregulated or downregulated genes. (**E**) qPCR validation of select tDRG differentially expressed genes identified in the 1 dpi and 4 dpi RNA-seq data from SARS-CoV-2-infected male hamsters. Each gene's expression is reported relative to that of a reference gene (*Actb*) and normalized to its expression in tDRG from mock-infected hamsters. Each gene's fold change (F.C.) as determined by RNA-seq, for comparison, is noted below. *$P < 0.05$, ****$P < 0.0001$ by multiple t-tests. Data are mean ± SEM from n

= 3 to 8 animals per group. **(F)** IPA-predicted upstream regulators of the gene changes in the RNA-seq data from 1 and 4 dpi tDRGs from SARS-CoV-2-infected or IAV-infected male hamsters. Figure is representative of the combination of data from n = 4 animals per group. *$P < 0.05$ by Benjamini-Hochberg analysis.
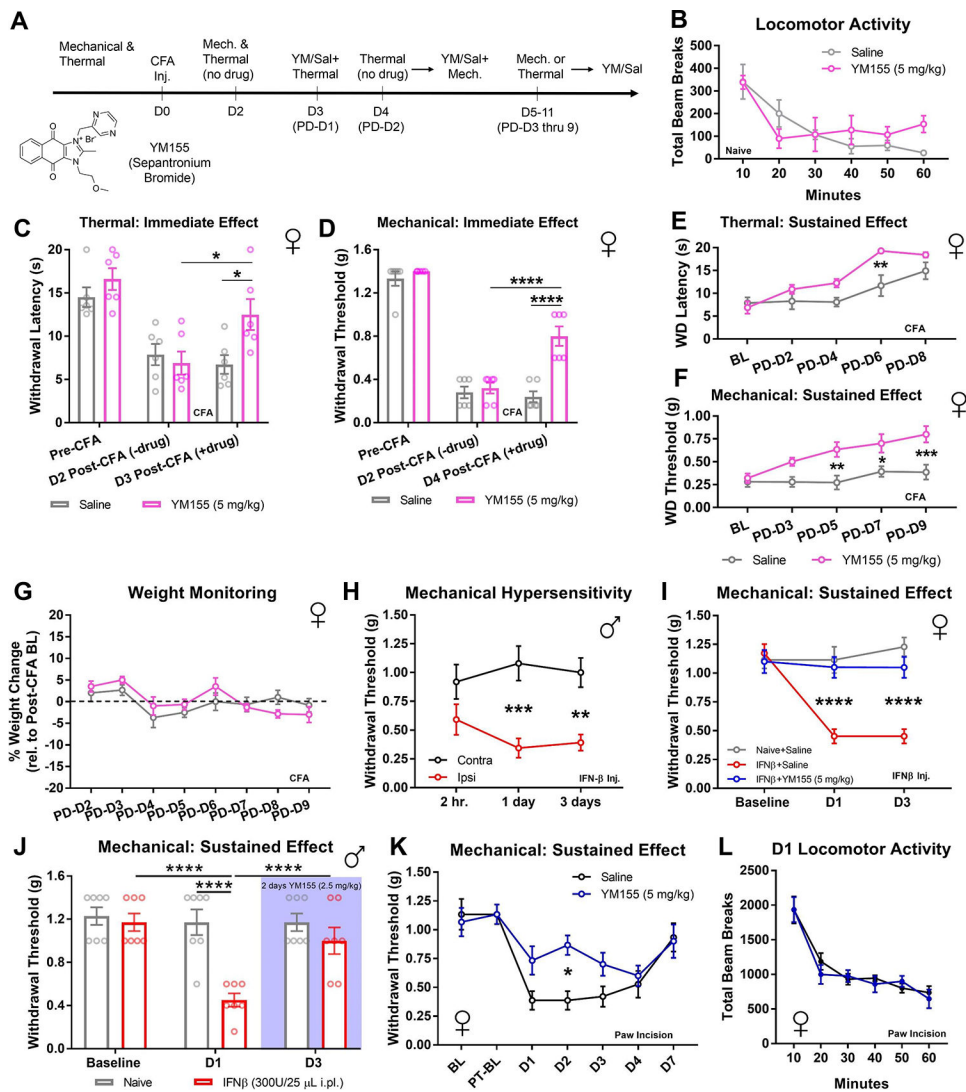
Figure 4. YM155 alleviates CFA-induced thermal and mechanical hypersensitivity in an immediate and sustained fashion.

(**A**) CFA assay timeline enabling behavioral testing of immediate and prolonged behavioral effects of YM155. D0 through D11 = day 0 through day 11. PD-D1 through PD-D9 = post-drug (YM155 or saline) day 1 through post-drug day 9. (**B**) Beam break locomotor assay in female mice (naïve; no CFA), assessed at intervals 10 to 60 min after treatment with either saline or YM155 (5 mg/kg); n = 5 to 6 animals per group. Differences not statistically significant by two-way ANOVA with Sidak's m.c. tests. (**C and D**) Thermal and mechanical sensitivity thresholds in female mice before hindpaw CFA injection (Pre-CFA), 2 days after CFA [D2 Post-CFA(-drug)], and either 3 days (for thermal) or 4 days (for mechanical) after CFA and 30–60 min after administration of either saline or YM155 (5 mg/kg i.p. daily), referring to the timeline in (A). Data are mean ± SEM from n = 6 animals per group in both panels. *$P < 0.05$ and ****$P < 0.0001$ by two-way ANOVA Sidak's m.c., see also table S2. (**E and F**) Effect of YM155 (5 mg/kg) on thermal and mechanical sensitivity thresholds in female mice described in (C and D), at later time points, referring to the timeline in (A). BL = baseline, at "D2" (no drug). n = 6 animals per group in both

panels. $*P < 0.05$, $**P < 0.01$, $***P < 0.001$ by two-way ANOVA Sidak's m.c., see also table S2. **(G)** Weight of CFA-injected female mice over the course of administration of saline or YM155 (5 mg/kg), referring to the timeline in (A). **(H)** Effect of hindpaw injection of IFN-β (300U in 25 μL) on contralateral versus ipsilateral mechanical hypersensitivity in male mice at the post-injection times indicated (hr. = hours). Data are mean ± SEM from n = 5 animals per group. $**P < 0.01$, $***P < 0.001$ by two-way ANOVA Sidak's m.c., see also table S2. **(I)** Effect of YM155 treatment (5 mg/kg i.p.), initiated at the time of IFN-β injection and continued through day 3 (D3), on mechanical hypersensitivity induced by hindpaw injection with IFN-β (300U in 25 μL) in female mice. BL = prior to IFN-β and YM155 administration. Data are expressed as mean ± SEM from n = 7 to 8 animals per group. $****P < 0.0001$ by two-way ANOVA Sidak's m.c., see also table S2. **(J)** Effect of two daily administrations of YM155 (2.5 mg/kg i.p.) initiated after Day 1 of IFN-β injection on mechanical hypersensitivity in male mice three days after hindpaw injection of IFN-β (300U in 25 μL). Data are mean ± SEM from n = 7 animals per group. $****P < 0.0001$ by two-way ANOVA Sidak's m.c., see also table S2. **(K)** Effect of pre-treatment with YM155 (5 mg/kg i.p. once-daily for seven days after BL, before PT-BL measurements) on mechanical hypersensitivity in female mice after paw incision. BL = pre-treatment baseline; PT-BL = thresholds after YM155 administration, pre-paw incision; D1 to D7 = days after paw incision. Data are expressed as mean ± SEM from n = 6 animals per group. $*P < 0.05$ for two-way ANOVA Sidak's m.c., see also table S2. **(L)** Locomotion observed over the course of an hour on the day after paw incision in mice pretreated with YM155 (blue) or saline (black). Data are from n = 6 animals per group.
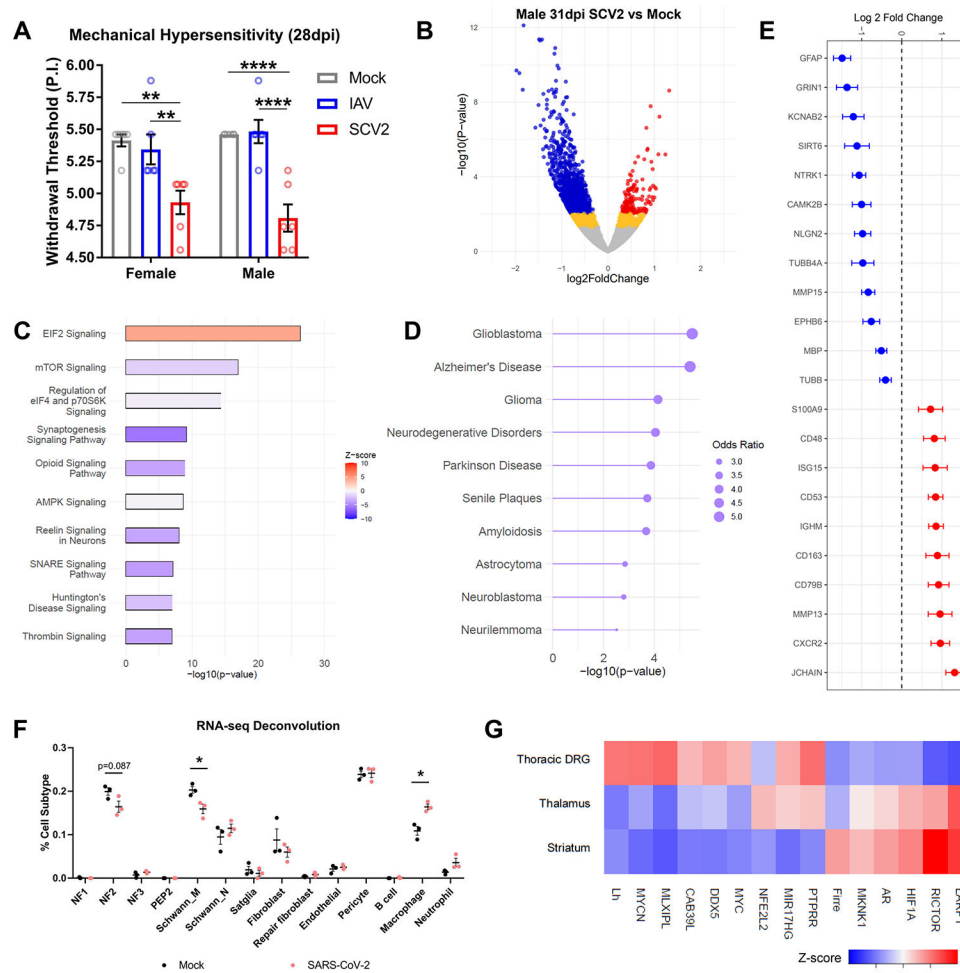
Figure 5. SARS-CoV-2 infection results in substantially reduced mechanical thresholds and a neuropathic transcriptomic landscape in the tDRGs well after viral clearance.

(**A**) Mechanical thresholds of mock-, IAV-, and SARS-CoV-2-infected female and male hamsters at 28 dpi. Data are mean ± SEM from n = 6 female and 6 male hamsters per group. **P < 0.01 and ****P < 0.0001 by one-way ANOVA Tukey's m.c., see also table S2. P.I. = linear perceived intensity. (**B**) Volcano plot of RNA-seq data from tDRGs from SARS-CoV-2-infected male hamsters at 31 dpi. Figure is representative of combined n = 3 per group. Red = *P*-adj. < 0.1, log2FC > 0; blue = *P*-adj. < 0.1, $\log_2$FC < 0; yellow = *P*-nom. < 0.05. (**C**) Top 10 canonical pathways by IPA (-$\log_{10}$(*P*-value) > 1.3) associated with the differentially expressed genes (DEGs) from the hamsters described in (B). *P*-nom. < 0.05. (**D**) Enrichr DisGENET gateway-derived top 10 diseases associated with the DEGs from the animals described in (B). *P*-nom. < 0.05. (**E**) Log_2 fold change (FC) of select neuronal and inflammatory genes from the 31 dpi RNA-seq data described in (B). *P*-adj. < 0.1. (**F**) Cell type/subtype deconvolution of the RNA-seq data of tDRGs from the above male mock- and SARS-CoV-2-infected animals at 31 dpi. NF1/2/3 = low-threshold mechanoreceptors; PEP2 = peptidergic nociceptors; Schwann M and N refer to myelinating and non-myelinating subtypes; Satglia = satellite glial cells. *P < 0.01 by multiple t-tests, see also table S2. (**G**) Predicted increased or decreased activity of IPA-derived, top-15 URs from an association

analysis of the 31 dpi tDRG RNA-seq data described in (B), and thalamic and striatal brain tissue from male hamsters under the same conditions (Brain data combined from N = 4 animals per group) in a previously reported study (34) DEG *P*-nom. < 0.05.
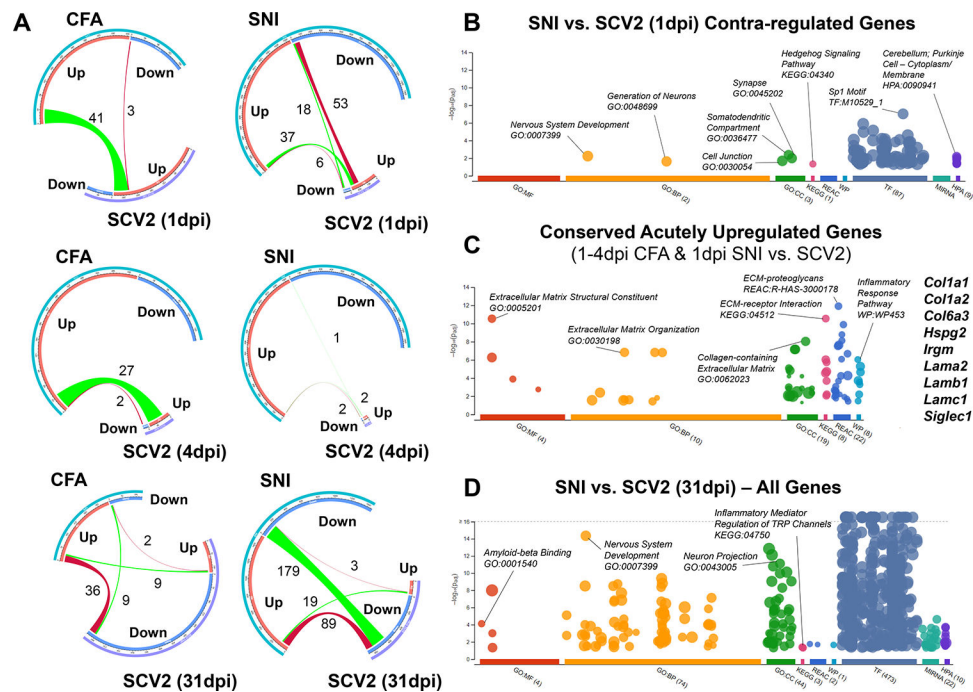
Figure 6. SARS-CoV-2 infection causes a longitudinally variable tDRG transcriptomic profile that shares pro-nociceptive components yet demonstrates unique plasticity signatures.

(**A**) Chord diagrams of gene expression changes in the tDRG assessing links between those regulated in mice by CFA or SNI with those regulated in hamsters by SARS-CoV-2 infection 1, 4, and 31 dpi. CFA and SNI, N = 3 female mice per group; SARS-CoV-2 1 and 4 dpi, N = 4 male hamsters per group; SARS-CoV-2 31 dpi, N = 3 male hamsters per group. (**B-D**) Dot plots presenting the identification of statistically significant (-$\log_{10}$ P-adj. > 1.3) gene ontologies (GO), pathways (KEGG, Kyoto Encyclopedia of Genes and Genomes; REAC, Reactome; WP, WikiPathways), transcription factors (TF, Transfac), microRNAs (MIRNA, miRTarBase), and tissue/cell expression profiles (HPA, Human Protein Atlas) associated with contra-regulated genes (B), conserved acutely upregulated genes (C), and among all genes (D) in the tDRG between the groups indicated, described in (A). Dot plots are adapted from g:Profiler. GO terms: MF, Molecular Function; BP, Biological Process; CC, Cellular Compartment.